

Cosentino Nicolas, Juan (Orcid ID: 0000-0001-9023-2726)  
Ruiz-Etcheverry Laura, Agustina (Orcid ID: 0000-0003-2570-1199)  
Coppo Renata (Orcid ID: 0000-0003-3968-1117)  
Saraceno Martin (Orcid ID: 0000-0002-5657-4420)  
Gaiero Diego, M. (Orcid ID: 0000-0003-1029-2265)

## **Does Satellite Chlorophyll-a Respond to Southernmost Patagonian Dust? A Multi-Year, Event-Based Approach**

**N. J. Cosentino<sup>1,2,3,4</sup>, L. A. Ruiz-Etcheverry<sup>5,6,7</sup>, G. L. Bia<sup>1,2</sup>, L. E. Simonella<sup>8</sup>, R. Coppo<sup>1,2</sup>, G. Torre<sup>1,2</sup>, M. Saraceno<sup>5,6,7</sup>, V. M. Tur<sup>1,2</sup>, and D. M. Gaiero<sup>1,2</sup>**

<sup>1</sup>Consejo Nacional de Investigaciones Científicas y Tecnológicas (CONICET), Centro de Investigaciones en Ciencias de la Tierra (CICTERRA), Universidad Nacional de Córdoba, Argentina.

<sup>2</sup>Facultad de Ciencias Exactas, Físicas y Naturales, Universidad Nacional de Córdoba, Argentina.

<sup>3</sup>Instituto de Geografía, Facultad de Historia, Geografía y Ciencia Política, Pontificia Universidad Católica de Chile, Chile.

<sup>4</sup>Núcleo Milenio Paleoclima, Chile.

<sup>5</sup>CONICET - Universidad de Buenos Aires, Centro de Investigaciones del Mar y de la Atmósfera (CIMA), Buenos Aires, Argentina.

<sup>6</sup>Universidad de Buenos Aires, Facultad de Ciencias Exactas y Naturales, Departamento de Ciencias de la Atmósfera y los Océanos (DCAO), Buenos Aires, Argentina.

<sup>7</sup>CNRS – IRD – CONICET – UBA. Instituto Franco-Argentino para el Estudio del Clima y sus Impactos (UMI 3351 IFAECI), Buenos Aires, Argentina.

<sup>8</sup>Facultad de Ciencias Químicas, Universidad Nacional de Córdoba, Argentina.

Corresponding author: Diego M. Gaiero (diego.gaiero@unc.edu.ar)

### **Key Points:**

- We present the first decadal time series of surface dust mass flux in Patagonia
- The first event-based study in the southwestern Atlantic Ocean shows no evidence for an influence of dust on chlorophyll-a concentrations
- Source-inherited low concentrations of bioavailable iron preclude enhancement of primary producers' biomass in proximal open ocean waters

This article has been accepted for publication and undergone full peer review but has not been through the copyediting, typesetting, pagination and proofreading process which may lead to differences between this version and the Version of Record. Please cite this article as doi: 10.1029/2020JG006073

## Abstract

Mineral aerosols may affect global climate indirectly by enhancing net primary productivity (NPP) upon deposition to the oceans and associated atmosphere-to-ocean CO<sub>2</sub> flux. This mechanism is hypothesized to have contributed significantly to the last interglacial-to-glacial climatic transition. However, the dust-NPP connection remains contentious for the present-day climate system. We analyze the impact of southernmost Patagonian dust emissions on southwestern Atlantic Ocean continental shelf and proximal open ocean satellite chlorophyll-a concentration. We use the first decadal time series of surface dust mass flux in southern Patagonia, along with in situ visibility data, to model dust emission, transport and deposition to the ocean. We then perform a dust event-based analysis of chlorophyll-a time series, using a novel approach by which time series are corrected for post-depositional particle advection due to ocean currents. Finally, we performed chemical analysis of iron in dust samples, a key micronutrient limiting phytoplankton biomass in high-nutrient, low-chlorophyll oceans such as offshore of the 200-m isobath off Patagonia. We find no compelling evidence for an influence of dust as an enhancer of phytoplankton biomass either on shelf or proximal open ocean waters of the southwestern Atlantic Ocean. For open ocean waters this is consistent with a lack of source-inherited bioavailable iron in dust samples. Future case studies addressing similar questions should concentrate on dust sources with identified high contents of bioavailable iron, particularly in the Southern Hemisphere where atmospheric processing of iron is weak.

## 1 Introduction

Mineral aerosols (i.e., dust) impact global climate through a number of mechanisms, including hypothesized atmosphere-to-ocean CO<sub>2</sub> flux due to enhancement of ocean net primary productivity (NPP) through input of micronutrient iron (Fe) to high-macronutrient, low-chlorophyll (i.e., HNLC) oceans (Martin, 1990; Moore et al., 2001). It has been proposed that this process may have contributed to the up to ~80 ppm atmospheric *p*CO<sub>2</sub> deficit during the globally dustier Last Glacial Maximum compared to the current interglacial (Martin, 1990). The identification of rises in NPP associated with present-day dust deposition would constitute a partial confirmation of this hypothesis.

Globally, the dust-NPP connection has been studied extensively using varying approaches, with some studies having found a positive correlation (e.g., Bishop et al., 2002; Gallisai et al., 2016; Shaw et al., 2008; Young et al., 1991), while most have found none (e.g., Baker et al., 2007; Bonnet et al., 2008; Crispo et al., 2005; Johnson et al., 2003; Mackie et al., 2008; Mills et al., 2004; Moore et al., 2006; Sedwick et al., 2005; Torfstein and Kienast, 2018; Westberry and Siegel, 2006). The open ocean waters south of ~45°S constitute the most extensive of the HNLC regions, and southern South America its main dust contributor, particularly to the Atlantic Ocean sector, both for the present-day (Li et al., 2008) and last glacial-interglacial cycle (Gili et al., 2017; Walter et al., 2000). It is thus of particular interest to test the role of dust as a NPP enhancer for the southern South America - southern Atlantic Ocean system (Bullard et al., 2016). Chlorophyll-a concentration ([Chl-a]) in the southern Atlantic Ocean is closely related to well-known oceanic phenomena, such as upwelling along the Patagonian shelf break (e.g., Carranza et al., 2017; Matano and Palma, 2008; Saraceno et al., 2005), tidal fronts (e.g., Romero et al., 2006) and open ocean

mesoscale features (e.g., Saraceno et al., 2005; Saraceno and Provost, 2012). Yet, dust deposition could have a superimposed effect on NPP in this region, and thus quantifying the relative contribution of dust to observed [Chl-a] is relevant.

In the Atlantic sector of the southern oceans, only three studies have looked at the dust-NPP connection, none of which analyzed individual dust events. Between ~40-55°S, Erickson III et al. (2003) found a strong positive correlation between dust deposition fluxes obtained from a global climate model and monthly-resolved, satellite-derived [Chl-a] for two years of data, which they ascribed to the influence of Patagonian-derived atmospheric Fe. A similar conclusion was reached by Cassar et al. (2007) based on similarly derived Fe deposition fields and measurements of net community production. Instead, Meskhidze et al. (2007) diminished the role of dust as a NPP enhancer by proposing that the correlation observed by Erickson III et al. (2003) could be explained in terms of the existence of an atmospheric circulation pattern in the region that simultaneously causes Patagonian dust uplift and deposition and upwelling of nutrient-rich waters. In turn, Boyd and Mackie (2008) question the use of atmospheric Fe models in the southern oceans due to lack of validation with Fe deposition observations. Given the uncertainties in modeled dust emission that persist for southern South America (Ohgaito et al., 2018; Takemura et al., 2009; Yukimoto et al., 2012) and the dominant role of oceanic processes on [Chl-a] dynamics in this region, the methodology that maximizes the chances of capturing any potential impact of dust on NPP is one in which a big number of dust events spanning multiple years are analyzed individually, each with constrained emission area and strength, where [Chl-a] after each dust event is compared to their specific pre-event background value.

Whereas total Fe content in dust and dust-emitting topsoils varies globally between 1-7 wt% (Gaiero et al., 2003; Guieu et al., 2002; Journet et al., 2008; Mahowald et al., 2005; Simonella et al., 2014, 2015), fractional Fe solubility (i.e., FFS) varies by more than four orders of magnitude (~0.001-90%) (Baker et al., 2006, 2013; Mahowald et al., 2005; Simonella et al., 2014, 2015). While part of this wide range in solubility estimates is explained by the equally wide range in techniques used (Perron et al., 2020), other factors include the mineralogical composition (e.g., Cwiertny et al., 2008; Journet et al., 2008) and Fe speciation (e.g., Shoenfelt et al., 2017) of dust at the source, and atmospheric processing (e.g., Hand et al., 2004). In the southern Atlantic Ocean, dust FFS ranges between 2.4-20% (Baker et al., 2006, 2013). In southern South America, three studies analyzed Fe on surface sediments believed to be the precursors of dust exported to the ocean (Shoenfelt et al., 2017; Simonella et al., 2014, 2015), with FFS measurements between 0.01-4.5% (Simonella et al., 2014, 2015). In terms of dust close to sources in southern South America, there is an almost complete dearth of Fe studies, with a single sample analyzed by Simonella et al. (2015). Given the uncertainty in soluble Fe of dust, particularly for that exported from southern South America, it is important that total Fe content and FFS be constrained in studies that analyze the effect of individual events of dust deposition on ocean NPP.

Here, we present the first decadal time series of present-day surface vertical and horizontal dust mass flux in southern Patagonia. We use this data set together with hourly-resolved visibility data to model dust emission, transport and deposition to the southwestern Atlantic Ocean for 32 dust events in a 6-yr period. Next, we constructed

time series of satellite [Chl-a] to gauge the response of phytoplankton biomass to dust deposition for each event for the first time in this region. Finally, we determine the total Fe concentration, surface Fe speciation and perform release experiments under different pH conditions to evaluate some aspects of Fe bioavailability of the dust aerosol samples. We find that post-dust event [Chl-a] signals are for the most part unaffected by dust deposition, consistent with low concentrations of soluble Fe and high Fe<sup>3+</sup> (versus Fe<sup>2+</sup>) in the analyzed dust samples.

### 1.1 Dust sources in southernmost Patagonia

The study area is located in the northern sector of Tierra del Fuego island, off the southern tip of Patagonia (Figure 1a). The region is semi-arid, dominated by grasslands and shrublands. Low hill ranges punctuate the landscape and define endorheic basins whose depositional centers collect superficial run-off channelized through short and ephemeral streams (Figure 1b) (Villarreal & Coronato, 2017). These depositional centers are deflation hollows, many of which contain a seasonal, shallow water body that accumulates during the months of positive hydrologic balance when precipitation exceeds evaporation (April-August). Hydrologic deficit begins in September, which together with year-round strong southwesterly winds is conducive to aerial exposure of easily erodible fine-grained lake bed sediments along their western margin (Figure 1c), in turn leading to dust emissions mainly during the austral summer (Figure 1d-e).

### 1.2 Background biological activity and chemistry of the southwestern Atlantic Ocean

We look at satellite-derived surface ocean [Chl-a] to gauge the effect of dust on phytoplankton biomass. Even if this presents caveats such as a phytoplankton physiology-dependent chlorophyll-biomass relationship (Geider et al., 1997) and the fact that satellites are limited to the first optical depth (i.e., depth at which sunlight irradiance is reduced to  $1/e$  of its surface value), [Chl-a] remains the best proxy for phytoplankton biomass (Huot et al., 2007). Because dust emission in southernmost Patagonia occurs mostly during the austral summer, we look at the January-February-March climatology of [Chl-a] (Figure 2a) to analyze background phytoplankton biomass. Within the continental shelf, values range between 0.4-1.0 mg m<sup>-3</sup>, while [Chl-a] in the southwestern Atlantic Ocean open ocean waters drop to <0.2 mg m<sup>-3</sup>.

Available summer surface ocean macronutrient concentration data (World Ocean Atlas 2018) show south-to-north reductions for nitrate (Figure 2b), phosphate (Figure 2c) and to a lesser degree silicate (Figure 2d). This reflects the influence of macronutrient-rich subantarctic waters on the southwestern Atlantic Ocean nutrient stocks. Superimposed to this trend, there is a rise in nitrate from continental shelf to open ocean waters (Figure 2b). North of 55°S, silicate is found at low concentrations both in the shelf and open ocean (Figure 2d). The fact that continental shelf waters are high-chlorophyll and low-macronutrient in summer, particularly north of 52°S, is best explained by prolonged consumption of nutrients by phytoplankton since the end of light-depleted conditions in late winter, and eventual nutrient depletion in summer.

Very few dissolved surface Fe measurements exist in open ocean waters of the southwestern Atlantic Ocean, with no measurements at all within the continental shelf (Figure 2e). There is also limitation in terms of time coverage, given that data is only available for one late austral summer (45-55°S) and for one early fall (55-60°S)

GEOTRACES oceanographic campaigns (Schlitzer et al., 2018). Available observations indicate predominantly low dissolved Fe, with concentrations  $<0.49$   $\text{nmol kg}^{-1}$ , which is the threshold value required to persist throughout the mixed layer during at least three days to initiate an algal bloom in the Fe-limited Southern Ocean (Boyd et al., 2010).

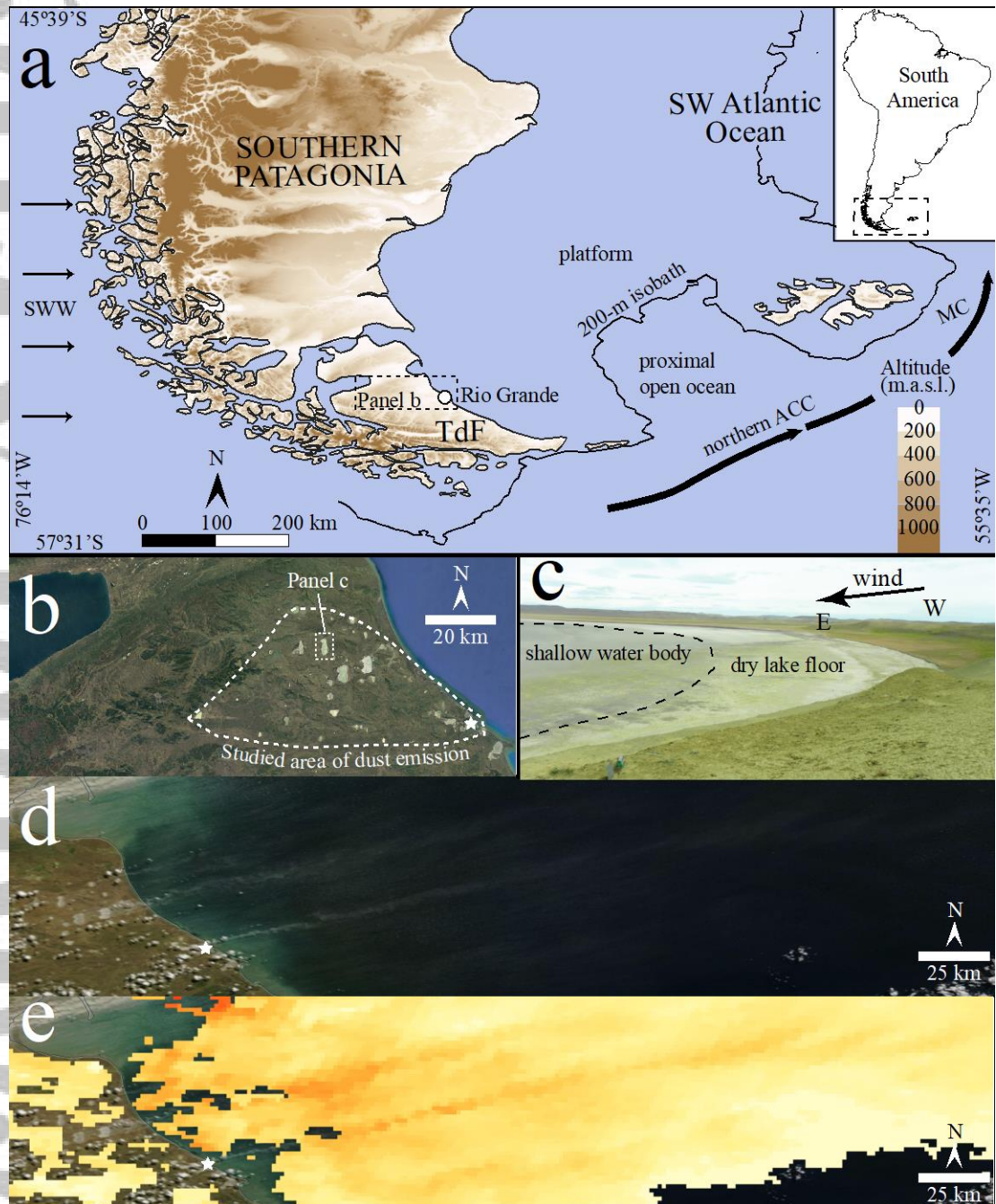


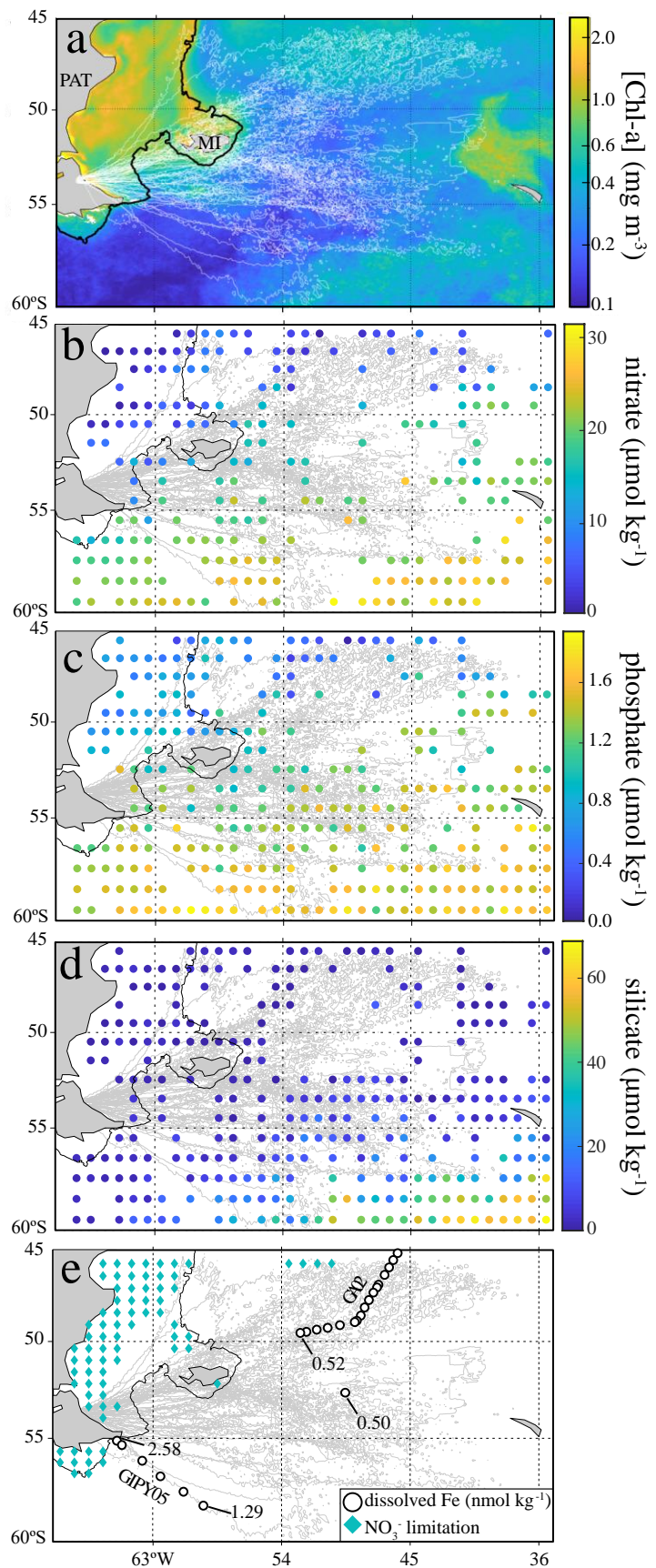
**Figure 1.** (a) Digital elevation model (SRTM, 90 m) of southern Patagonia, including Tierra del Fuego (TdF). SWW: South Westerly Winds, MC: Malvinas Current, ACC: Antarctic Circumpolar Current. (b) Satellite image (Landsat/Copernicus) of the study area, showing the area of dust emission analyzed in this study. (c) Deflation pan showing a windward dry lake floor and a leeward shallow water body (modified from Villarreal and Coronato, 2017). (d) True color Terra/MODIS image of a dust event on 21 February 2014, where two dust plumes emitted from the study area are identified.

(e) These plumes are clearly defined by higher-than-background Aerosol Optical Depth (Terra/MODIS). White star: Rio Grande dust monitoring station.

Biogeochemical modeling agrees with available observations. Song et al. (2016) used a model with six biogeochemical tracers and a representation of the dependency of the biological uptake of  $\text{NO}_3^-$  and Fe as a function of nutrient and light availability, to conclude that between 45-55°S the Patagonian shelf is mostly nitrate-limited during summer, while open ocean waters are mostly Fe-limited (Figure 2e).

Accepted Article

**Figure 2.** Austral summer (JFM) concentrations of (a) chlorophyll-a (2013-2019, OC-CCI v4.2) and (b,c,d) major macronutrients (<10 m depth, 1°-grid cell means, World Ocean Atlas 2018) in the southwestern Atlantic Ocean. (e) Dissolved Fe measurements (<10 m below sea level) as part of GEOTRACES cruise sections GA02 (March 2011) and GIPY05 (April 2008) (Schlitzer et al., 2018). Dots with no tag <math>0.49 \text{ nmol kg}^{-1}</math>. Cyan diamonds represent areas where nitrate is modeled to be the limiting nutrient (vs. Fe), with Fe the limiting nutrient elsewhere (Song et al., 2016). White/grey contours correspond to modeled  $5 \mu\text{g m}^{-3}$  isolines of total dust deposition for the 32 dust events considered in this study (see section 3.2). The black contour is the 200-m isobath. PAT: Patagonia, MI: Malvinas Islands.



## 2 Materials, Data and Methods

### 2.1 Dust sampling

Dust was sampled using two passive collectors installed on the outskirts of Rio Grande city (53.79°S, 67.75°W) (Figure 1). One collector is a pyramidal receptacle (CP), with a 2025-cm<sup>2</sup> collection surface suited for measuring vertical dust flux (e.g., Cosentino et al., 2020a; Gaiero et al., 2003, 2013; Orange et al., 1990; Skonieczny et al., 2011). The other is a Buffalo Spring Number Eight (BSNE) (Fryrear, 1986), with a 10-cm<sup>2</sup> collection surface suited for measuring horizontal dust flux (e.g., Cosentino et al., 2020a; Waza et al., 2019). Both collectors were placed 5 m above ground to avoid collecting local saltation material. They trapped particles during 38-day average sampling periods, after which an operator collected the samples using a vacuum pump to filter particles on a previously weighted 0.45 μm membrane.

### 2.2 Constraining dust event length with visibility data

Visibility and wind speed data from the Argentine meteorology agency at World Meteorological Organization (WMO) station #87934 (distant <1 km from the dust monitoring site) are used to constrain the duration of individual dust events (see Table S1 of the Supporting Information). Hourly resolved dust events are defined based on reductions in visibility due to dust-related phenomena (from a normal 30-km visibility to an average of 5.6 km during dust events). Dust phenomena is reported as Present Weather international surface synoptic observation (i.e., SYNOP) codes 6-9, 30-35 and 98 (Table S1). As expected, events were associated with short-term rises in wind speed (see Figure S1 of the Supporting Information). This is consistent with the general observation that high wind speed triggers dust emission (e.g., Gillette et al., 1980) and supports the use of visibility data for in situ dust event identification (e.g., Gaiero et al., 2013; Gassó et al., 2010; Gassó and Torres, 2019).

### 2.3 Grain size measurements

Dust deposition is a function of grain size. Grain size distributions (GSDs) of samples of dust exported to the ocean (i.e., BSNE samples) were measured by laser-diffraction using a Horiba LA-950 particle size analyzer. Samples were minimally dispersed to prevent the breaking up of aggregates. The reproducibility of measurements was tested using mixtures of glass beads (NIST Traceable polydisperse particle standard PS202/3–30 μm and PS215/10–100 μm, Whitehouse Scientific). For both runs (PS202, n = 6 and PS215, n = 5), the median (D50) and D10/D90 percentiles were within 3% and 5% of the certified nominal values, respectively.

### 2.4 Modeling of dust emission, transport and deposition

The Hybrid Single Particle Lagrangian Integrated Trajectory Model version 4 (HYSPLIT4) was used to model particle emission, atmospheric dispersion, and deposition (Draxler & Hess, 1998) for each dust event. The National Center for Environmental Prediction's Global Data Assimilation System meteorological grids (Kanamitsu, 1989) were used, with 3-hour and 0.5° resolutions. It has been shown that air-parcel trajectories based on wind fields from these climate reanalysis data are robust, showing high correlations to measurements at high-latitude Southern Hemisphere stations (Neff and Bertler, 2015). Also, this model has been extensively

used to characterize dust and volcanic ash events on a regional scale in southern South America (e.g., Bucher and Stein, 2016; Gaiero et al., 2013; Gassó et al., 2010; Simonella et al., 2015).

Particle diameter was prescribed as the mode of the GSD of the corresponding BSNE sample. If more than one mode exists, then as many particle diameters as existing modes were defined, with mass apportionment based on the GSD. Particle shape was assumed spherical and density was set to  $2650 \text{ kg m}^{-3}$ , except for particles with diameter  $<1 \text{ }\mu\text{m}$  for which density was set to  $2500 \text{ kg m}^{-3}$  (Li et al., 2008).

To constrain the emission surface area for individual dust events, backward particle dispersion was first performed with a point source located at the dust monitoring site. Total simulation time was set as the duration of the dust event. Dust concentration was then time-integrated within 0-1500 meters above ground level, with the concentration contour equivalent to two orders of magnitude less than the concentration maximum used as a spatial boundary within which dust-emitting surfaces were mapped. An example of this procedure for one dust event analyzed is shown in Figure 3a-b. The concentration gradient along the direction perpendicular to the main advection direction was generally steep and thus the results are not sensitive to the choice of dust concentration contour. Surfaces were mapped on a collection of high-resolution true color satellite images by CNES/Airbus and Maxar Technologies (displayed by Google Earth). The historical collection of satellite imagery from Google Earth was used to differentiate exposed surfaces for each dust event.

For the forward trajectory simulation, a point dust emission source was assumed, estimated by visual inspection for each dust event (Figure 3b). The extent of dust deposition ( $>1000 \text{ km}$  from the coast) is more than an order of magnitude greater than the distance between the most distant dust-emitting surfaces considered ( $\sim 70 \text{ km}$ ) (Figure 3c), which justifies this simplification. Given the proximity of the BSNE collector to the emitting surfaces, it is assumed that horizontal dust flux during any given BSNE sampling period is equal to the dust emission rate. It is further assumed that all BSNE dust mass collected during any given sampling period was accumulated during dust-related visibility reduction events (i.e., dust events), and that background dust (i.e., dust accumulated outside of dust events) contributed negligibly (see section 3.1 for a justification of this assumption). To calculate dust emission rate for each dust event, each BSNE sample total mass was apportioned to each dust event based on the intensity and length of the reduction in visibility.

In HYSPLIT4, dry deposition is achieved through gravitational settling, while wet deposition is achieved through below-cloud and in-cloud processes when grid cells have a non-zero precipitation value and a defined cloud layer (Draxler & Hess, 1998). Default below-cloud and in-cloud parameters were used for dust deposition (both  $8 \times$

$10^{-5} \text{ s}^{-1}$ ). Finally, simulations are run for 24 hours, after which dust deposition is found to be negligible.

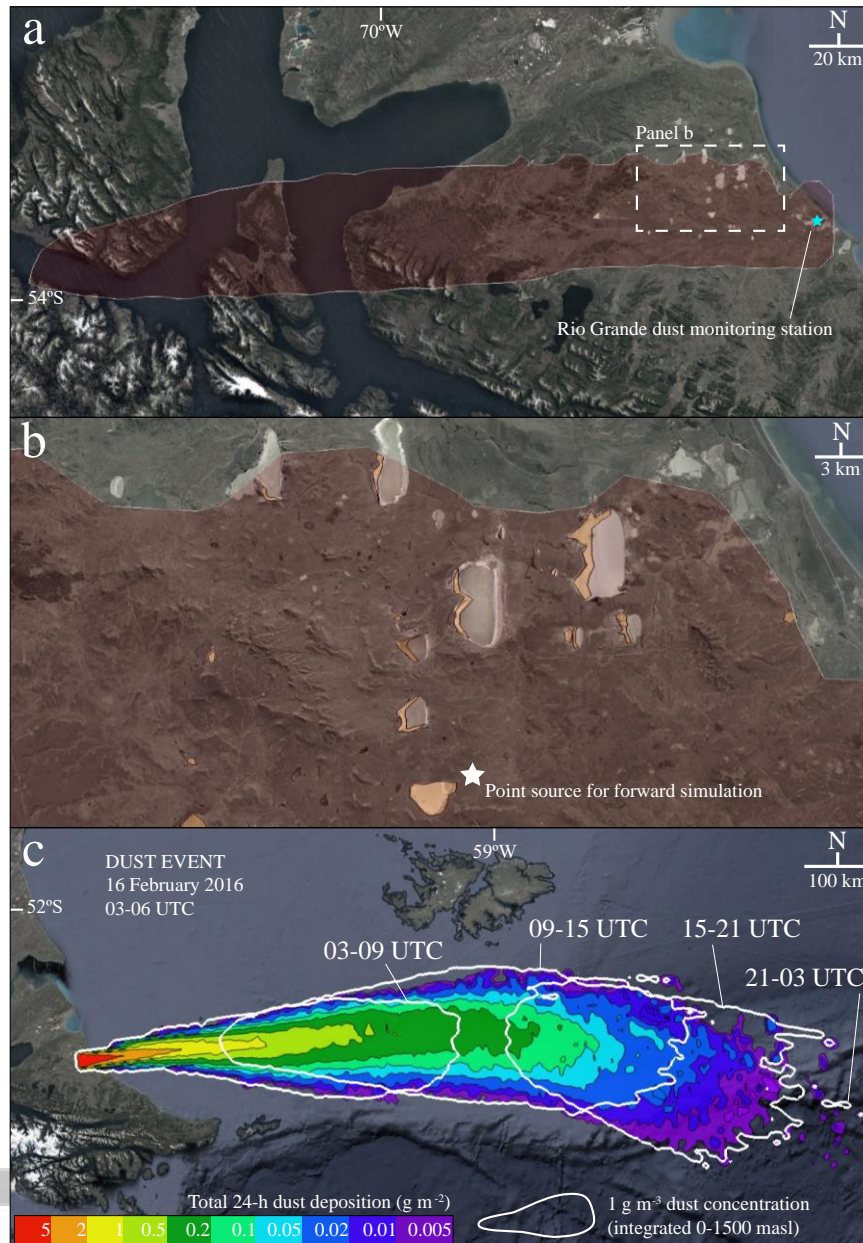


**Figure 3.** (a) Backward dispersion simulation for a 3-hour dust event with point-source emission from the BSNE collector at the monitoring station. (b) Mapping of dust sources within the contour defined by backward dispersion. (c) The forward dispersion simulation.

### 2.5 Satellite [Chl-a] time series

Surface [Chl-a] data was obtained from the Ocean Colour - Climate Change Initiative version 4.2 (OC-CCI v4.2). This product has a 4-km spatial resolution and is constructed by merging all available satellites (MERIS, Aqua-MODIS, SeaWiFS and VIIRS) (Sathyendranath et al., 2019). This product was chosen over any single satellite so as to reduce the amount of missing values due to clouds, which is an issue in the study region (e.g., Romero et al., 2006). To further reduce missing data, 5-day

composite values were used (Figure 4a), which constitutes a good compromise between data completeness and the loss in temporal resolution, given expected response times of [Chl-a] to input of dust of >6 days (Tian et al., 2018). Next, a mask was applied between the coast and 80-m depth to remove pixels whose signal is contaminated by suspended material, and where the tidal regime is strong enough to mix the entire water column (Rivas & Pisoni, 2009), bringing nutrients from the bottom and potentially masking the atmospheric-induced [Chl-a] signal. Four search areas were defined based on bathymetry (i.e., shelf vs. open ocean, limited by the 200-m isobath) and intensity of time-integrated dust deposition (i.e., HYSPLIT-derived deposition contours): the area (1) onshore of  $0.2 \text{ g m}^{-2}$ , (2) onshore of  $0.02 \text{ g m}^{-2}$ , (3) offshore of  $0.02 \text{ g m}^{-2}$  and (4) offshore of  $0.005 \text{ g m}^{-2}$ .

Four [Chl-a] time series were built for each dust event, one for each of these four search areas, where each data point is the 5-day spatial average of pixels within the search area. Figure 4b shows an example of a [Chl-a] time series whose search area is onshore of the time-integrated  $0.2 \text{ g m}^{-2}$  deposition contour. Data points are considered only when at least 50% of the pixels comprising a search area contain data. We classify each post-event data point as equivalent (E), high (H) or low (L) based on whether they fall within, above or below a 95%-confidence interval built around the average of the pre-event signal (one month), respectively. For details on how we modify this methodology for pre-event signals that trend, or for time and/or spatially overlapping dust events, see Text S1 of the Supporting Information.

Given the possibility that ocean fertilization by dust is either not instantaneous or protracted, surface ocean current advection of deposited dust particles was considered using satellite altimetry. The main shelf circulation in the region is to the NE with velocities that increase from the coast ( $\sim 0.03 \text{ m s}^{-1}$ ) to the shelf break ( $\sim 0.4 \text{ m s}^{-1}$ ) where the strong northward Malvinas Current flows (e.g., Palma et al., 2008; Rivas, 1997). South of  $54^\circ\text{S}$ , the Antarctic Circumpolar Current has a mean velocity of  $\sim 0.8 \text{ m s}^{-1}$  (Koenig et al., 2014). Here, velocities were calculated from gridded maps of satellite-derived sea surface height (Copernicus Marine and Environment Monitoring Service) with 1-day and  $0.25^\circ$  resolutions. Altimeter-derived currents account only for the geostrophic component of the currents. Yet, comparisons with in situ measurements show that they represent very accurately ocean currents in the region (Barré et al., 2008; Ferrari et al., 2012). Backward and forward trajectories were calculated using the Runge Kutta fourth order method (Mehdi & Kareem, 2017). The position of dust particles after 8-12 days of being deposited on 12 February 2018 is observed in Figure 4a. Then, we extracted the nearest [Chl-a] values in terms of space and time, and averaged spatially for each time step to construct the time series corrected for current advection.

## 2.6 Total concentration, release experiments and solid speciation analysis for Fe

The  $<63\text{-}\mu\text{m}$  size fraction of most of the collected dust samples represent over 90% of total sample volume and hence, chemical analyses described in this section were run on bulk dust samples. Total Fe concentration of the six BSNE collector dust samples representing peaks in dust flux was determined by alkaline fusion at  $1050^\circ\text{C}$  using  $\text{Li}_2\text{B}_4\text{O}_7$  (Spectromelt A10), followed by dissolution with sub-boiled  $\text{HNO}_3$  5%. A blank sample composed purely of lithium tetraborate was included to correct for matrix Fe concentration. Finally, resulting dissolutions were analyzed by inductively coupled plasma - optical emission spectrometry (ICP-OES, Thermo Fisher Scientific

iCAP 7200). The validity of this methodology was tested by determining total Fe for two reference materials during the same run: granodiorite USGS GSP-2 (Wilson, 1998) and river sediment SRM 2704 (Epstein et al., 1989).

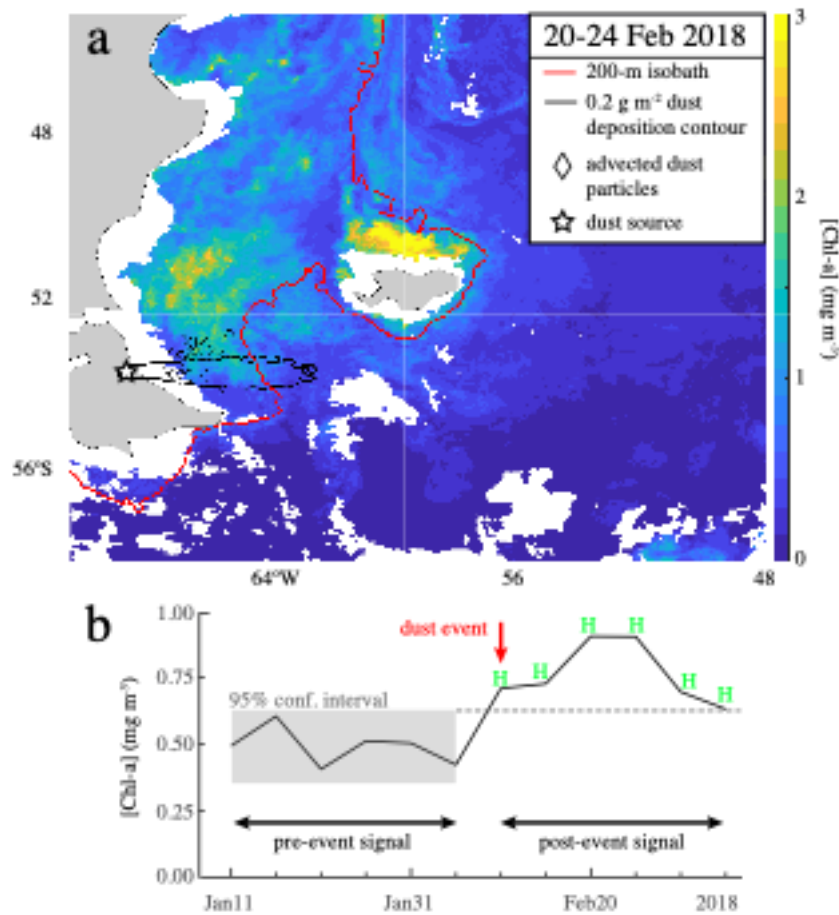


**Figure 4.** (a) Map of [Chl-a] for 20–24 February 2018. The black diamonds represent the final position of dust particles after advection by satellite ocean currents from the day of the dust event to 20 February 2018. (b) Time series for [Chl-a] uncorrected for post-depositional dust particle advection due to surface ocean currents. All six 5-day mean values after dust deposition plot above the 95% confidence interval of the pre-event signal, so they are classified H for “high”.

The release of Fe in dust samples was evaluated with a continuous flow method. A solution extraction stream was propelled by a peristaltic pump (Gilson Minipuls 3) at  $0.880 \pm 0.005 \text{ mL min}^{-1}$  through a column that contained the dust sample ( $\sim 5.00 \text{ mg}$ ), as well as a methodological blank (i.e., no sample). The supernatant was collected in an acid-washed tube. The leaching experiment consisted of two steps. First, a flow of deionized water (MilliQ, pH $\sim 5$ ) passed through the column for 20 minutes. Deionized extraction is intended to measure Fe in the most labile surface mineral phases. It was observed that 20 minutes were enough for removing the easily available Fe from similar samples (Simonella et al., 2014). The second step consisted of extraction with a diluted acid solution (sub-boiled HNO<sub>3</sub> 1%, pH $\sim 2$ ) which passed through the system for 80 minutes. This is intended to measure Fe in water-insoluble surface mineral phases. In a similar study, a fast Fe release after 30–40 minutes of sample contact with HNO<sub>3</sub> 1% was observed, after which the dissolved Fe concentration increased at a slower rate (Simonella et al., 2015). Iron concentration in the supernatants retrieved

after each step were determined by ICP-OES. See Cosentino et al. (2020b, 2020c) for procedural details on ICP-OES runs for both total Fe and Fe release experiments (i.e., analytical blank results, blank corrections, run controls, duplicates, curve calibration, detection and quantification limits, reproducibility and error analysis).

The surface speciation of Fe (2–10 nm) in dust samples was determined by X-ray photoelectron spectroscopy (XPS, Thermo Fisher Scientific K-Alpha+). To minimize charging effects, samples were bombarded during data acquisition with low-energy electrons supplied by a flood gun, and three spectra of the same element with no evidence of beam damage were collected (Bia et al., 2020). Besides, the spectrum of C 1s, O 1s and Si 2p were monitored from the beginning to the end of measurements in order to determine the extent of the charging effect. Spectra for C 1s and Fe 2p were fitted using theoretical parameters from Wagner et al. (1997) and the XPSPeak 4.1 software. Further details can be found in Text S2 of the Supporting Information.

### 3 Results and discussion

#### 3.1 A 10-yr record of episodic dust emissions from southernmost Patagonia

Dust activity as measured by dust-related visibility reduction during the last decade (Table S1) peaks during the austral summer months: an average of 0.8 to 2.5 days per month experienced a dust event during January to March, with a secondary peak in spring (Figure 5a). The rest of the year is characterized by a dearth of events. This annual variability is similar to that observed by Gassó and Torres (2019) in a coastal site in central Patagonia (~46°S). Mean annual precipitation (see Table S2 in the Supporting Information) is 341 mm, reaching maximums during summer (Figure 5a). Notably, the month with highest mean precipitation coincides with the peak in number of dust events (February). However, when potential evapotranspiration is considered, it is observed that both peaks in dust activity take place during months of negative hydrological balance, and in particular, the main peak occurs after six (out of seven) months of water deficit have elapsed. Wind is persistent throughout the year, with maximum monthly-mean speeds of 7.5–8.3 m s<sup>-1</sup> during spring. The secondary peak in dust event occurrence takes place during the month of highest wind speed (November). Winds are controlled by the South Pacific anticyclone, resulting in dominant W-SW, W and W-NW directions (Figure 5b). During dust events, mean wind speed is 14.6 m s<sup>-1</sup> ( $WS_{mean}$ ), with most events characterized by wind speed above 11.2 m s<sup>-1</sup> ( $WS_{mean} - 1\sigma$ ). For events occurring during the main (secondary) peak in January–February–March (November),  $WS_{mean}$  and  $WS_{mean} - 1\sigma$  are 14.5 (15.7) and 11.2 (12.5) m s<sup>-1</sup>, respectively. We may thus consider 11.2 and 12.5 m s<sup>-1</sup> as surface wind speed thresholds for dust emission downwind of the dust monitoring site under summertime and spring soil moisture conditions, respectively. A higher wind speed threshold during November than during summertime is consistent with a shorter cumulative time of negative hydrological balance (Figure 5a), which implies higher soil moisture.

Vertical dust flux (i.e., deposition rate) as measured by the CP collector between December 2008 and February 2019 (no data between August 2010 and September 2011) averages 0.27 g m<sup>-2</sup> day<sup>-1</sup> (95% of samples: 0.00–0.27 g m<sup>-2</sup> day<sup>-1</sup>) (Figure 5c). This average is highly influenced by three samples between August–November 2015 that constitute exceptionally high mass accumulation. Discarding them, the average vertical dust flux is 0.08 g m<sup>-2</sup> day<sup>-1</sup>. The high and irregular sampling interval

(average: 38 days, 15-168 days) makes it difficult to ascertain any annual variability, precluding traditional statistical trend tests and spectral analysis (e.g., Cosentino et al., 2020a). However, visual inspection indicates no annual periodicity. A compilation of global dust deposition rates spanning diverse methodologies and meteorological conditions shows a relationship between deposition rate and distance to sources, in which sites located >1000 km (global), between 10 and 1000 km (regional), and <10 km (local) from source regions receive  $0.05\text{--}1\text{ g m}^{-2}$ ,  $1\text{--}50\text{ g m}^{-2}$  and  $>50\text{ g m}^{-2}$  of airborne dust per year, respectively (Lawrence and Neff, 2009). Our mean deposition rate ( $99\text{ g m}^{-2}\text{ yr}^{-1}$ , or  $27\text{ g m}^{-2}\text{ yr}^{-1}$  excluding the August-November 2015 peak) is consistent with this global dataset, given that sources contributing dust to the CP collector at the Rio Grande monitoring station are located <70 km (see next section).

Horizontal dust flux (i.e., in transit) as measured by the BSNE collector between December 2008 and February 2019 averages  $12\text{ g m}^{-2}\text{ day}^{-1}$  (95% of samples:  $0.00\text{--}49\text{ g m}^{-2}\text{ day}^{-1}$ ) (Figure 5d). Measured masses for each sampling interval for both the BSNE and CP collectors, as well as grain size measurements, can be found in Cosentino et al. (2020d). Contrary to the CP time series, horizontal dust flux clearly shows an annual seasonality, peaking in austral summer and late spring. Mean surface dust concentration is  $22\text{ }\mu\text{g m}^{-3}$ . The only other study that measured in situ surface dust concentration in Patagonia was carried out by Crespi-Abril et al. (2018), albeit with a different methodology (i.e., high-volume, active sampler). No mean is reported in the Crespi-Abril et al. (2018) study, but by visual inspection a December 2004 to December 2007 mean of  $\sim 45\text{ }\mu\text{g m}^{-3}$  is estimated for a coastal site in northern Patagonia ( $42.8^\circ\text{S}$ ), roughly twice our estimate.

Notably, dust events are clustered within peaks in BSNE horizontal dust flux (Figure 5d). Also, the higher the number of dust events and/or the longer their duration, the higher the peak in BSNE dust flux. This is particularly evident for well-defined BSNE peaks (i.e., with short sampling periods). This observation, together with the fact that BSNE dust flux outside major peaks is comparatively small, justifies our assumption

that most of the mass collected at the BSNE trap was accumulated during dust events, with mass accumulated by background dust activity negligible.

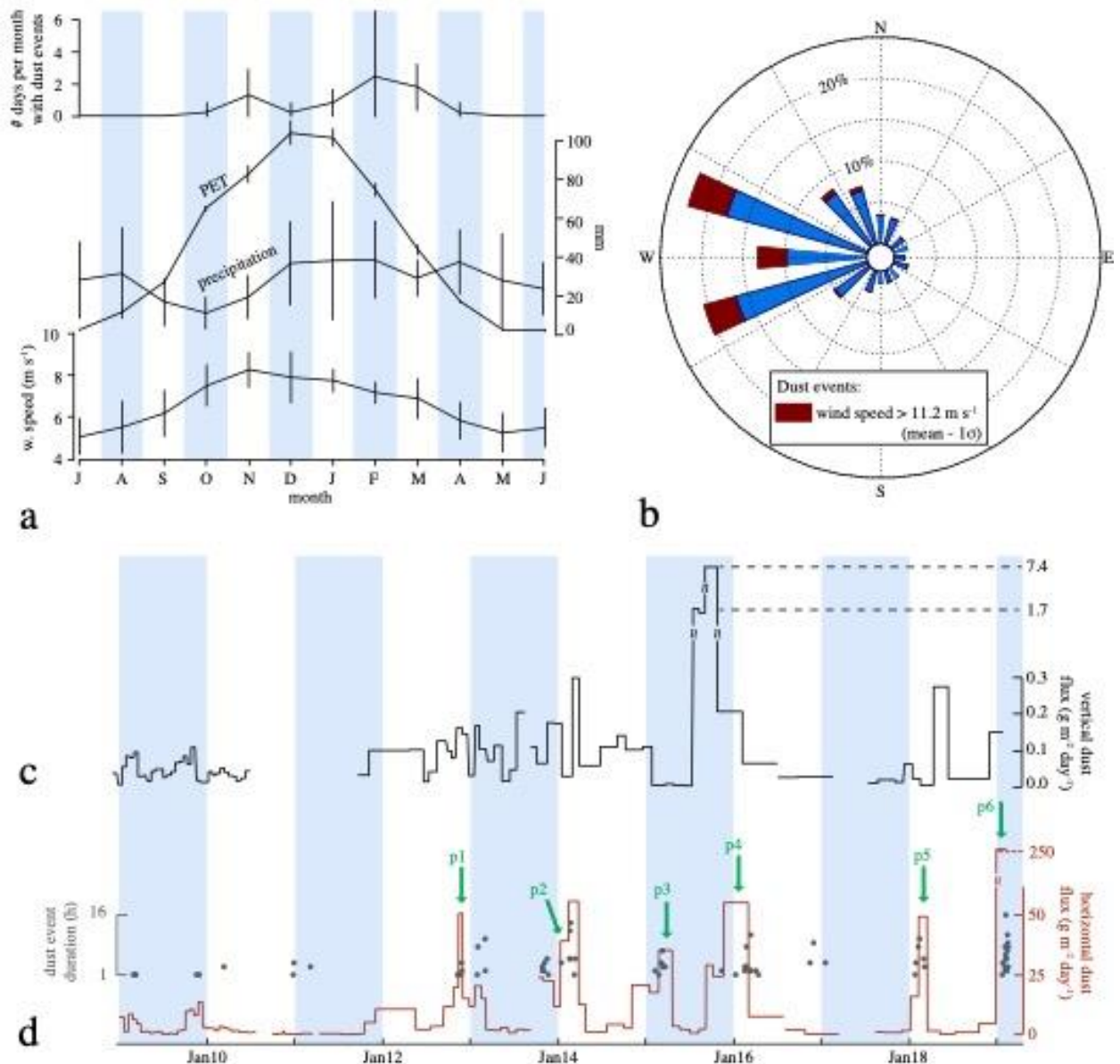


**Figure 5.** (a) Monthly means for days per month with at least one hour of reduction in visibility due to dust (January 2009–February 2019), precipitation, potential evapotranspiration (PET, Penman-Monteith) and wind speed (January 2009–December 2018). Error bars are 1σ. (b) Direction of wind (hourly) between 29 December 2008 and 20 February 2019. Wind speed during dust events is mostly >11.2 m s<sup>-1</sup>. (c) Vertical and (d) horizontal dust fluxes measured at the dust monitoring station (red line), and visibility reduction events due to dust (i.e., dust events, black dots). The 32 dust events that fall inside peaks in horizontal dust mass

flux marked with green arrows were modeled in terms of particle trajectories and deposition.

### 3.2 Dust deposition on the southern Patagonian shelf and proximal open ocean

Between December 2008 and February 2019, 73 dust events, defined as a reduction in surface visibility due to dust, were identified at the Rio Grande city airport (Figure 5d). A subset of 32 dust events (see Table S3 of the Supporting Information), all taking place during peaks in horizontal dust flux at the Rio Grande monitoring station (see green arrows in Figure 5d) were simulated. Based on backward dispersion modeling, dust-emitting surfaces are located proximally to the monitoring station (<80 km). Individual events are associated with dust-emitting surface areas ranging between 8.3-78.4 km<sup>2</sup>, while emission rates range between 1.0-34.3 Gg h<sup>-1</sup> (Table S3). BSNE efficiency is between 35-45% with no (Goossens and Offer, 2000) or little (Waza et al., 2019) wind speed dependency between 1-5 m s<sup>-1</sup>. However, wind speed was above this range most of the time in Rio Grande, so that these emission rates should be considered minimum estimates.

Dust deposition during these 32 dust events (Figure 2) was controlled by prevailing northwesterly to southwesterly winds (Figure 5b), with a total deposition area of  $\sim 1.8 \times 10^6$  km<sup>2</sup> between 45-60°S (Figure 2). Dust was deposited over the continental shelf (onshore of the 200-m isobath) as well as over the open ocean waters of the southwestern Atlantic Ocean. An average of 72% of the total dust mass emitted from the study area from November 2012 to February 2019 was deposited within this vast area, with dust deposition rate at  $112 \pm 43$  Gg yr<sup>-1</sup>. Most dust deposition (71%) however took place proximally, within the southern Patagonian continental shelf and the open ocean waters surrounding the Malvinas archipelago (Figure 2a).

### 3.3 Links between surface ocean dust deposition and [Chl-a]

We analyzed [Chl-a] time series of Patagonian shelf and proximal open ocean waters for a month before and after 32 dust events originating in southernmost Patagonia. Emissions were concentrated during the austral summer and spanned >6 years. Most post-event 5-day-mean [Chl-a] data points across all studied dust events and dust deposition contours fall within the pre-event variability, both within the shelf (Figure 6a, see also Table S4 of the Supporting Information) and open ocean (Figure 6b, Table S4).

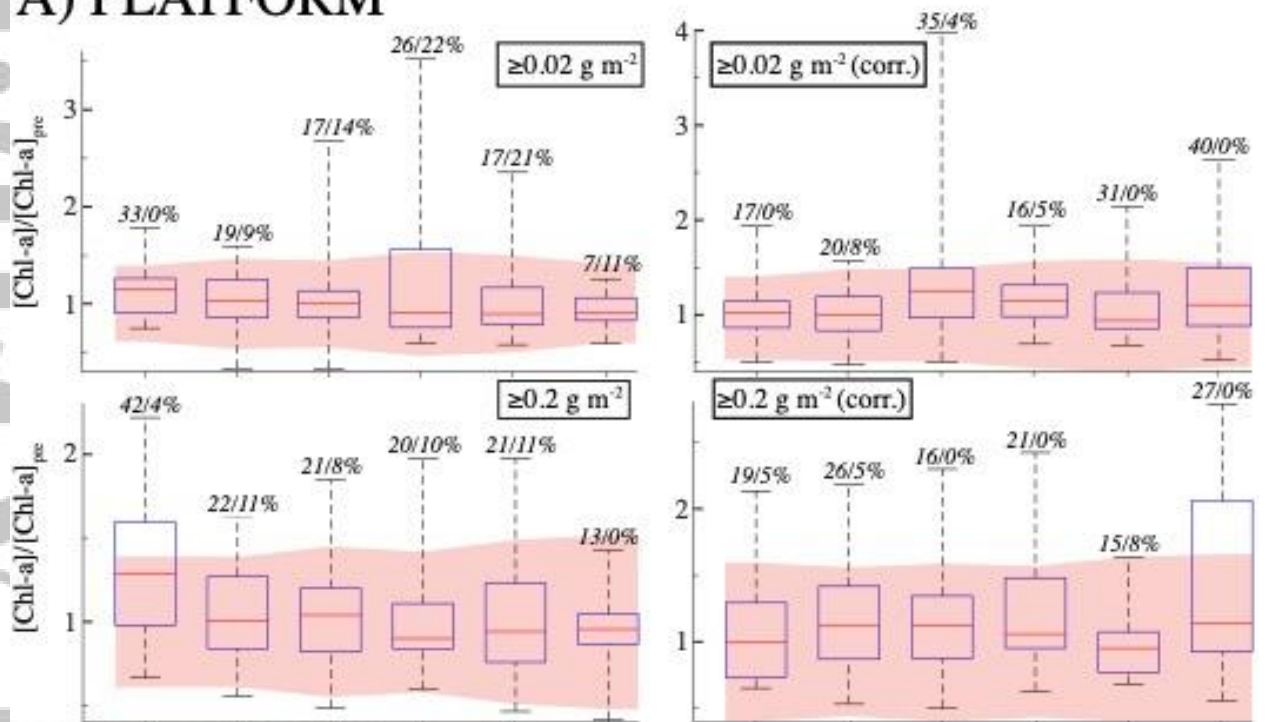
Within the shelf and for [Chl-a] uncorrected for advection, [Chl-a] data points that classify as H (i.e., higher than pre-event signal) dominate over those classifying as L (i.e., lower than pre-event signal). This is true for the area of time-integrated dust deposition  $\geq 0.02$  g m<sup>-2</sup> (7-33% vs. 0-22%), and more so for the area of dust deposition  $\geq 0.2$  g m<sup>-2</sup> (13-42% vs. 0-11%) (Figure 6a). Data points classified as H are concentrated on days 1-5 after dust deposition, particularly for the area of higher deposition, where 42% of data points classify as H (vs. 54% and 4% that classify as E and L, respectively). An example of this behavior is illustrated in Figure 7a, which shows the [Chl-a] time series for a search area defined by the  $\geq 0.2$  g m<sup>-2</sup> time-integrated deposition contour for dust event p6e9 (Table S3). Here, [Chl-a] for the 5-day period that includes the day in which dust deposition took place is significantly above the pre-event signal, even accounting for the observed trend. To test whether this short-term rise in [Chl-a] may have been triggered by dust deposition, we look at

a map of anomalies of [Chl-a] of days 1-5 after the dust event with respect to the pre-event signal (i.e., [Chl-a] for days 1-5 minus mean pre-event [Chl-a]) (Figure 7b). A broad positive [Chl-a] anomaly is observed within the shelf, but rather than being restricted to the area of dust deposition it extends all along the Tierra del Fuego shelf waters. Dust emission surfaces similar to the ones considered here extend north of the study area in Tierra del Fuego and the rest of southern Patagonia. Arguably, rises in surface wind speed conducive to dust emission in our study area could also have generated emissions further north, as was the case on 26 February 2005 (Gassó et al., 2010). Assuming that dust deposition indeed enhances phytoplankton biomass within the Patagonian shelf, analogous dust emission sites located further north could potentially explain the broader spatial scale of positive [Chl-a] anomalies outside the dust deposition area projected from our sample site. However, for this event, the positive [Chl-a] anomaly extends further south and the dust emission sources considered in this study are the southernmost of its nature along the Patagonian coast. Another explanation for the broad positive [Chl-a] anomaly is that high wind speeds conducive to localized dust emission and deposition are also conducive to broader-scale water column mixing within the shelf and associated potential upwelling of nutrient-rich deep waters. In this scenario, the broad-scale positive [Chl-a] anomaly associated with wind-induced water mixing should be accompanied by a higher, localized positive anomaly in the area impacted by dust. This hypothetical second-order positive [Chl-a] anomaly cannot be distinguished from the broad-scale pattern in Figure 7b.

Offshore of the 200-m isobath, the opposite occurs, with [Chl-a] data points that classify as L dominating over those that classify as H ( $\geq 0.005 \text{ g m}^{-2}$ : 4-26% vs. 7-17%;  $\geq 0.02 \text{ g m}^{-2}$ : 4-35% vs. 4-11%) (Figure 6b). Contrary to the positive [Chl-a] anomaly over the shelf, the negative [Chl-a] response in open ocean waters is protracted and becomes more evident starting at days 11-15 after dust deposition. For dust particles deposited over the continental shelf, the error of not considering post-depositional ocean advection is small due to a low-velocity shelf circulation. Instead, dust particles deposited on proximal open ocean waters are subjected to the strong Malvinas current (Figure 1) and within 5-8 days they may be advected away from the deposition area. Given that the observed low post-event [Chl-a] signal is protracted, correction of the open ocean data set by ocean advection is warranted. The corrected [Chl-a] data set also shows a dominance of L over H data points, albeit not as strongly as the uncorrected data set, as well as a protracted response starting at days 11-15 after dust deposition (Figure 6b). Figure 7c shows a time series for [Chl-a] before and after the same dust event as Figure 7a, this time offshore of the 200-m isobath, that exemplifies this protracted negative anomaly starting at days 11-15 after dust deposition. Figures 7d-f show maps of [Chl-a] anomalies for days 11-15, 16-20 and 26-30 after dust deposition. East of the Malvinas islands and for these three time periods, [Chl-a] anomalies show negative values in a broad region that extends to the north and south of the dust deposition contour. The spatial pattern of this decrease in [Chl-a] does not correspond with the dust deposition contour and does not trail the path of advected particles. There is thus no compelling evidence for an influence of southernmost Patagonian dust on phytoplankton biomass at either shelf or proximal

open ocean waters of the southwestern Atlantic Ocean. Similar findings were reported for Australian dust events (Boyd et al., 2004).

## A) PLATFORM



## B) OPEN OCEAN

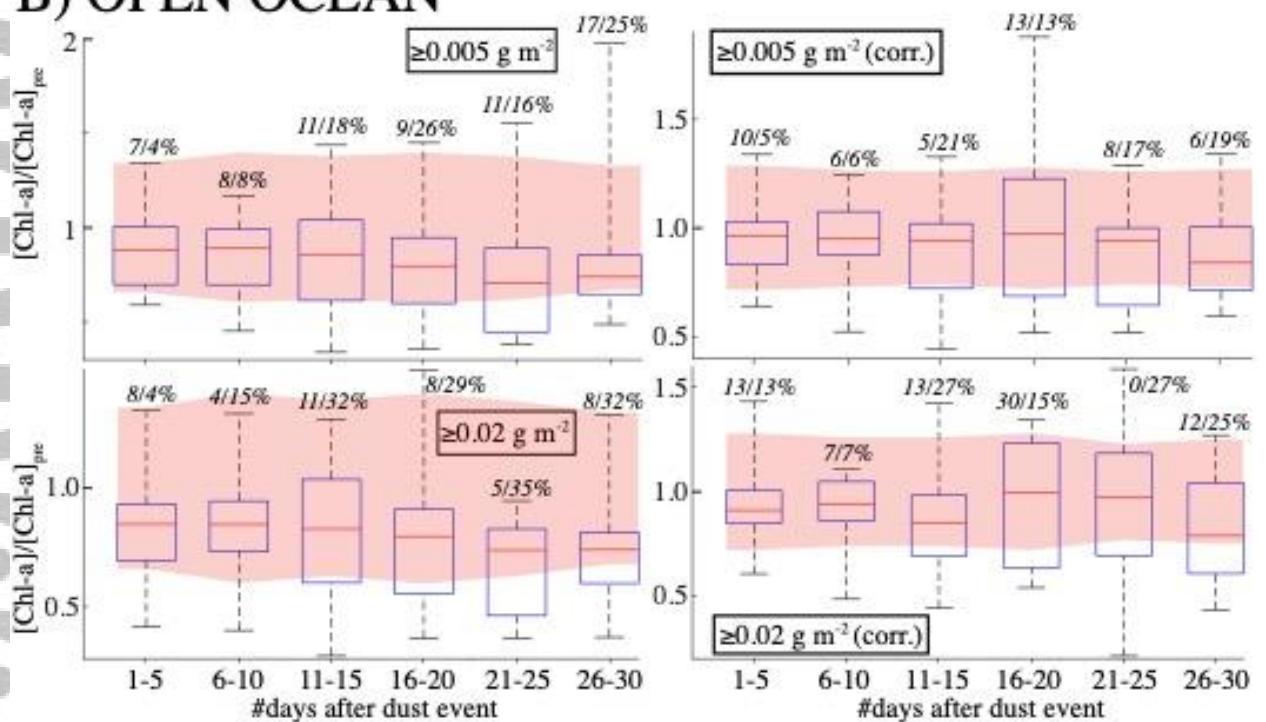


**Figure 6.** Summary of results of our satellite [Chl-a] analysis in southernmost Patagonia. We plot (a) platform (i.e., onshore of the 200-m isobath) and (b) open ocean area-averaged [Chl-a] for 5-day periods after dust deposition, normalized to the pre-event mean, within dust deposition contours of 0.005, 0.02 and 0.2  $\text{g m}^{-2}$ , with and without correction (corr.) for post-depositional particle advection due to currents. On

each box, the central red mark represents the median, the bottom and top blue edges indicate the 25th and 75th percentiles, respectively, and the whiskers extend to the most extreme data points. Data points separated more than  $3\sigma$  from the mean were previously discarded. The pink area represents the mean 95% confidence interval around the pre-event means. The percentages correspond to the fraction of dust events that classify as high (H)/low (L), with  $H + L + E$  (i.e., equivalent) = 100% (see section 2.5).

### 3.4 Low Fe bioavailability of dust at the source precludes [Chl-a] enhancement

Total Fe content for the six BSNE collector dust samples representing peaks in horizontal mass flux range between 2.77-3.23 wt% (Table 1), within the reported 1-5 wt% global variability (e.g., Mahowald et al., 2005). Six of seven topsoil samples collected from a variety of geomorphic locations believed to be present-day dust sources in Patagonia range between 1.8-3.3 wt% (Shoenfelt et al., 2017; Simonella et al., 2015), with one outlier at 16 wt% in northern Tierra del Fuego island (Shoenfelt et al., 2017). Only one dust total Fe measurement exists at a coastal site in northern Patagonia (i.e., 4.1 wt%, Simonella et al., 2015).

However, it is not total Fe content that acts as a main control on Fe bioavailability to planktonic biota, but rather the most labile fraction of Fe and solid speciation of materials at continental sources (e.g., Morel et al., 2008; Shoenfelt et al., 2017), atmospheric wet processing (e.g., Colin et al., 1990; Meskhidze et al., 2003) and post-depositional ocean processing (e.g., Maldonado and Price, 1999; Strzepak et al., 2011). We performed experiments to determine Fe solubility of dust samples in deionized water as a measure of the solubility of Fe that is inherited by dust from the source, previous to any atmospheric or oceanic processing. Values range between 0.00079-0.00420 wt% with respect to total sample (Table 1), or 0.03-0.15% in terms of FFS. These values of FFS are at the lower end of the ~0.001-90% global variability range, which includes FFSs not only under deionized water conditions, but under more acidic conditions as well.

Surface (i.e., first 2-10 nm) speciation of Fe in dust particles indicates a predominance of oxidized Fe(III) for the illuminated surfaces, with Fe(II) between 13-22% (vs. Fe(III), Table 1). XPS results are consistent with Fe(II)-O and Fe(III)-O chemical bondings. In accordance with values reported in the literature (Biesinger et al., 2011; Grosvenor et al., 2004), binding energies for Fe(II)-O at 709 eV and for Fe(III)-O at 711-712 eV suggest (hydr)oxides and silicates as the main Fe-bearing phases (see Figure S2 of the Supporting Information and Cosentino et al. (2020e) for further details). Although these mineral phases carrying Fe(II) and Fe(III) cannot be constrained any further with XPS alone, Fe(II) is in general more soluble and bioavailable than Fe(III) (Baker & Croot, 2010; Schroth et al., 2009; Shaked et al., 2005). This is consistent with low Fe solubility in deionized water. It is also consistent with the predominantly non-glacial origin of surface materials that emit dust in the study area (Villarreal & Coronato, 2017), which has been shown to be associated with higher Fe(III) than Fe(II) (Shoenfelt et al., 2017).

Source-inherited Fe solubility in dust may be enhanced by several proposed mechanisms during atmospheric transport and after deposition to the ocean. Some of these mechanisms include atmospheric acidification through oxidation of  $\text{SO}_2$  in the atmosphere (e.g., Colin et al., 1990), including  $\text{SO}_2$  derived from anthropogenic

emissions (e.g., Koch et al., 2000) and from the oxidation of dimethyl sulfide (DMS) emitted by phytoplankton (e.g., Duce & Tindale, 1991), as well as adaptive strategies by phytoplankton to access organically complexed Fe (e.g., Strzepek et al., 2011). In order to gauge Fe solubility enhancement due to any combination of these diverse phenomena, we performed experiments to measure the solubility of Fe in dilute acid (HNO<sub>3</sub> 1%). Although we have no means to test whether any of these mechanisms may be acting in the shelf and proximal open ocean waters of the southwestern Atlantic Ocean, we argue that solubility of Fe in dilute acid (HNO<sub>3</sub> 1%) may be used as an upper boundary estimate of Fe that is effectively bioavailable to phytoplankton. Acid-soluble Fe ranges between 0.148-0.207 wt% with respect to total sample (Table 1), or between 4.4-6.6% in terms of FFS. This represents a solubility enhancement of ~40-150x with respect to the deionized water leaching experiments. Nonetheless, it remains at the lower end of the global range in measured dust Fe solubility (i.e., ~0.001-90%).

Proximal open ocean waters impacted by dust deposition south of 50°S have high surface concentrations of macronutrients NO<sub>3</sub><sup>-</sup> and PO<sub>4</sub><sup>3-</sup> during austral summer, when dust events take place (Figure 2b-c). These waters are also characterized by low [Chl-a] (Figure 2a), constituting an HNLC region during summer. Available surface dissolved Fe measurements offshore of the 200-m isobath are scarce between 45-60°S and average 0.23 nmol kg<sup>-1</sup> (Figure 2e). These observations, together with biogeochemical modeling results (Song et al., 2016), are consistent with Fe being a limiting nutrient for phytoplankton growth, although it is possible that silicate may be a co-limiting macronutrient (Figure 2d). For dust events studied here, a conservative upper bound for the amount of dissolved Fe incorporated to open ocean waters through deposition of unprocessed dust (i.e., dust that did not experience Fe solubility enhancement due to atmospheric and/or oceanic processes) may be calculated assuming 0.2 g m<sup>-2</sup> time-integrated dust deposition, 0.00423 wt% dissolved Fe (Table 1) and a 20-m ocean mixed layer depth (see Figure S3 of the Supporting Information). Strong winds further north of our study area and west of the 200-m isobath generate intense vertical turbulence that readily homogenize the water column within the mixed layer depth in a matter of hours (e.g., Rivas & Piola, 2002). Winds are even stronger in the open ocean waters where dust from the studied events is deposited, so that vertical turbulence is arguably equally strong. It is thus estimated that <0.008 nmol L<sup>-1</sup> of dissolved Fe is added to open ocean waters through deposition of unprocessed dust, potentially raising background surface ocean values from ~0.22 nM to ~0.23 nM. This is insufficient to generate algal blooms in this region ([Chl-a] > 1 mg m<sup>-3</sup>), which require at least 0.5 nM along the full mixed layer depth for at least three days (Boyd et al., 2010). However, small inputs of Fe may have a resolvable effect on satellite [Chl-a]. By comparing post-event [Chl-a] with a pre-event background value that is specific to each of the multiple events our analysis maximizes the chances of capturing such small phytoplankton biomass responses. The fact that we do not see any response indicates that unprocessed dust iron deposition to the open ocean has an effect too small to be instrumentally resolved, or alternatively, that iron limitation relief cannot be achieved until a threshold value in Fe is reached.

An upper bound to dissolved Fe addition after atmospheric and/or ocean processing may be estimated if we instead use the maximum value measured for Fe solubility under acidic conditions (i.e., 0.208 wt%, Table 1). In this case an estimated ~0.4 nM may potentially be added, raising oceanic surface dissolved Fe concentration from

~0.2 nM to ~0.6 nM. Nonetheless, it is highly unlikely that processing of dust may raise Fe solubility for two reasons: (1) emissions of  $\text{SO}_2$  to the atmosphere derived from oxidation of DMS may not be sufficient to generate observable changes in NPP (Meskhidze et al., 2005), and (2) southernmost Patagonia is scarcely populated and local anthropogenic emissions of  $\text{SO}_2$  are negligible.

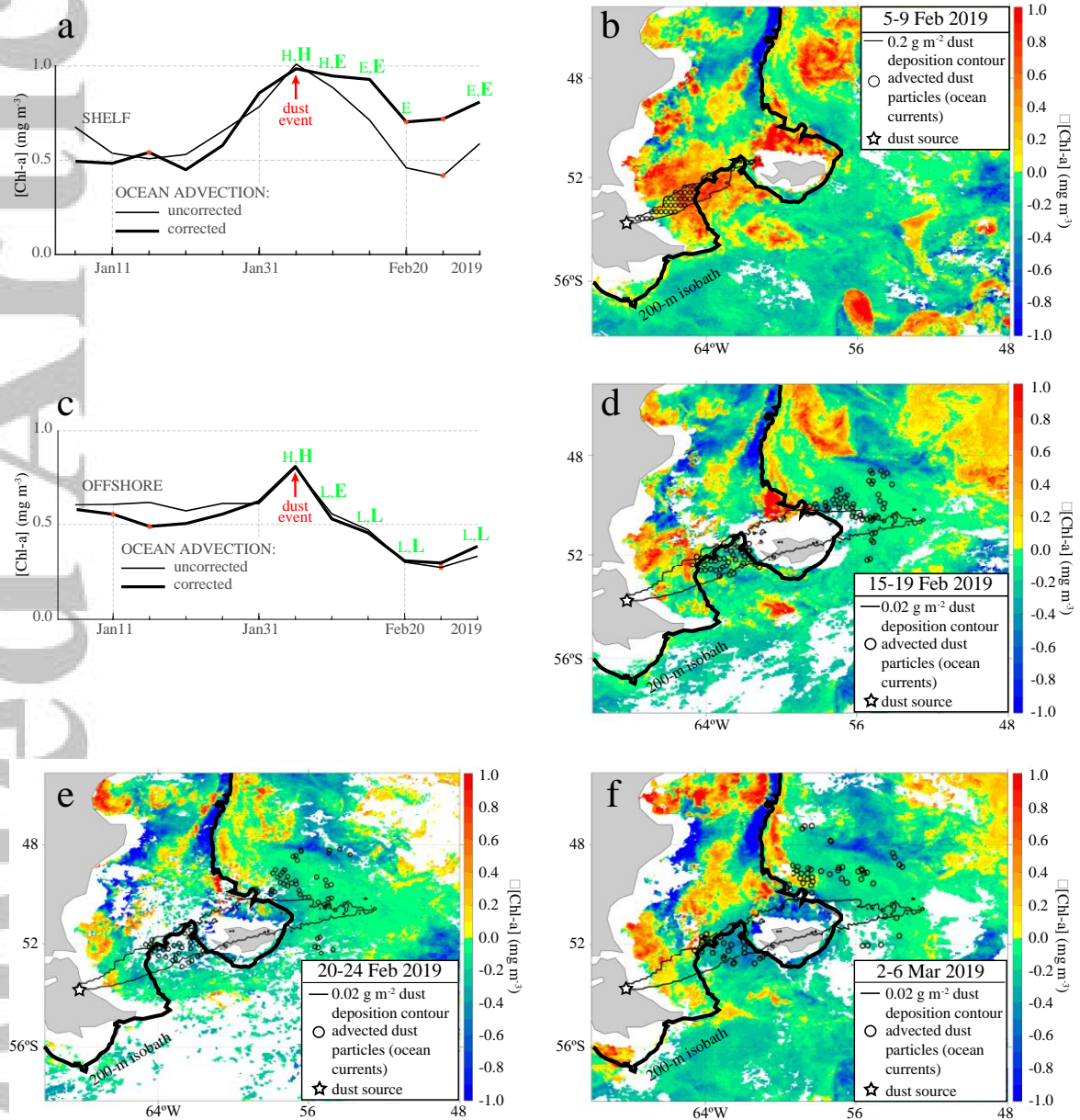


**Figure 7.** (a) Time series of [Chl-a] onshore of the 200-m isobath and within the  $0.2 \text{ g m}^{-2}$  time-integrated dust deposition contour, centered on the day of dust event p6e9 (Table S3). Green tags represent classification of data points based on pre-event signal variability (H: higher, E: equivalent and L: lower at 95% confidence level, normal (bold) text: data points uncorrected (corrected) for ocean advection). Red dots represent data-points that were obtained with less than 50% of pixels that fall within the search area. (b) Map of [Chl-a] anomalies for the 5-day period that includes the dust event, versus the mean of pre-event values (one month prior). (c) Same as (a) for a search area offshore of the 200-m isobath and within the  $0.02 \text{ g m}^{-2}$  time-integrated

dust deposition contour. (d-f) Same as (b) for the third, fourth and sixth post-dust event 5-day periods, respectively.

**Table 1.** Total iron ( $\text{Fe}_{\text{TOT}}$ ),  $\text{H}_2\text{O}$ - and  $\text{HNO}_3$ -soluble iron ( $\text{DFe}_{\text{w}}$  and  $\text{DFe}_{\text{acid}}$ ) and iron speciation ( $\text{Fe}^{2+}$  vs.  $\text{Fe}^{3+}$ ) of dust samples.

sample lab name	BSNE peak # <sup>1</sup>	$\text{Fe}_{\text{TOT}} \pm 1\sigma$ (wt%) <sup>2</sup>	$\text{DFe}_{\text{w}} \pm 1\sigma$ (wt%) <sup>2</sup>	$\text{DFe}_{\text{acid}} \pm 1\sigma$ (wt%) <sup>2</sup>	$\text{Fe}^{2+}$ (% vs. $\text{Fe}^{3+}$ ) <sup>3</sup>
RG-BSNE59	1	$2.83 \pm 0.02$	$0.00165 \pm 0.00001$	$0.148 \pm 0.001$	n.d.
RG-BSNE74	2	$2.77 \pm 0.01$	$0.00140 \pm 0.00001$	$0.188 \pm 0.001$	n.d.
RG-BSNE82	3	$3.137 \pm 0.004$	$0.00420 \pm 0.00003$	$0.183 \pm 0.001$	19
RG-BSNE89	4	$3.23 \pm 0.03$	$0.00295 \pm 0.00002$	$0.173 \pm 0.001$	16*
RG-BSNE99	5	$3.01 \pm 0.02$	$0.00079 \pm 0.00001$	$0.207 \pm 0.001$	15-21*
RG-BSNE104	6	$3.12 \pm 0.02$	$0.00176 \pm 0.00001$	$0.207 \pm 0.001$	13-22*

<sup>1</sup>See peak numbering in Figure 5d.

<sup>2</sup>With respect to total sample. For details see Cosentino et al. (2020b, 2020c, 2020e).

<sup>3</sup>CP collector samples analyzed for the same time period (asterisk). n.d.: no data.

Assessing the reasons for the lack of a response of phytoplankton biomass to dust deposition over Patagonian shelf waters is challenging due to a lack of data on dust macronutrient concentrations and surface Fe concentrations on the shelf (Figure 2e). Summer [Chl-a] over the section of the shelf most impacted by dust deposition (53-55°S) is low compared to shelf waters further north (<0.6 vs 0.4-1.0  $\text{mg m}^{-3}$ ) (Figure 2a). High  $\text{PO}_4^{3-}$  (Figure 2c) and low  $\text{NO}_3^-$  (Figure 2b) and silicate (Figure 2d) suggest co-limitation by  $\text{NO}_3^-$  and silicate. However, similarly low values in silicate elsewhere in the high-chlorophyll Patagonian shelf suggest silicate does not limit phytoplankton biomass in the shelf south of 53°S. No measurements exist for dissolved Fe in surface waters onshore of the 200-m isobath (Figure 2e), so that co-limitation by Fe cannot be assessed. The lack of surface ocean Fe measurements in this region also precludes validation of biogeochemical model results that suggest  $\text{NO}_3^-$  limitation at coastal and central shelf waters, and Fe limitation over the outer shelf waters (Song et al., 2016) (Figure 2e). In order to properly gauge the fertilization potential of dust in the Patagonian shelf, Fe determinations in dust should be complemented by similar macronutrient characterizations (Paparazzo et al., 2018).

#### 4 Conclusions

Based on a decadal time series of surface horizontal dust flux in situ observations and visibility data in southernmost Patagonia, we modeled dust emission, transport and deposition during 32 dust events sourced from exposed lake beds during austral summer. Dust was exported and deposited over the shelf and proximal open ocean waters of the southwestern Atlantic Ocean. An individual event-based analysis of [Chl-a] time series appropriate for identifying potentially small responses shows no compelling evidence for an influence of Patagonian dust deposition on satellite [Chl-a], neither on low-macronutrient, intermediate-chlorophyll shelf surface waters that are characteristic of the summer season nor on Fe-limited open ocean HNLC surface waters. The lack of phytoplankton biomass response to dust deposition on proximal open ocean waters is best explained by low Fe solubility of dust due to largely

insoluble Fe(III)-bearing phases inherited from the source regions, and a lack of atmospheric processing due to non-acidic atmospheric conditions in the region.

The so-called Fe hypothesis is a compelling explanation for the up to ~80 ppm atmospheric  $p\text{CO}_2$  surplus that existed during the last interglacial compared to the globally dustier Last Glacial Maximum. A partial confirmation for this hypothesis would be the identification of a single event-based connection between dust deposition to HNLC waters and phytoplankton biomass enhancement for the present-day climate system. We find that FFS inherited from dust source topsoils is key in determining mineral aerosol Fe bioavailability to ocean phytoplankton, particularly in the less industrialized Southern Hemisphere. Given the high variability of dust Fe solubility at the source, we find that similar future studies that look at the influence of dust on ocean NPP need to concentrate on dust events sourced from topsoils of identified high FFS. We also propose that in order to correctly gauge the impact of dust deposition on phytoplankton growth in waters with high-velocity surface currents, it is important to correct [Chl-a] time series for post-depositional dust particle advection.

## Acknowledgments

We thank C. Ferrer, G. Connon, L. Barbero and J. L. Hormaechea from Estación Astronómica Rio Grande (CADIC-CONICET) for continuous support with the dust monitoring program. We also thank Adi Torfstein and two anonymous reviewers for improving our manuscript with insightful comments. This work was financed by awards ANPYCT-PICT-2012-0525 and ANPYCT-PICT-2017-2705 to DMG, awards from SECyT-UNC, Antorchas, IAI, the Weizmann Institute and the Leverhulme Trust International Network to DMG, award ANID FONDECYT/POSTDOCTORADO 2020 #3200085 to NJC, and awards ANPYCT-PICT-2018-02433 and UBACYT 20020170100620BA to MS. The HYSPLIT4 model may be accessed online or downloaded (<https://www.ready.noaa.gov/HYSPLIT.php>). Ocean dissolved Fe data can be accessed through the GEOTRACES Intermediate Data Product 2017 (<https://www.geotraces.org/geotraces-intermediate-data-product-2017/>). Macronutrient ocean concentrations were obtained from the World Ocean Atlas 2018 (<https://www.nodc.noaa.gov/OC5/SELECT/woaselect/woaselect.html>). The [Chl-a] data is from OC-CCI v4.2 (<https://esa-oceancolour-cci.org>), while the ocean surface height data is from the Copernicus Marine and Environment Monitoring Service (<https://marine.copernicus.eu>). All new data generated in this contribution has been deposited in the EarthChem online repository, including: total iron and iron solubility of dust (Cosentino et al., 2020b, 2020c), dust mass and grain size (Cosentino et al., 2020d) and dust iron speciation (Cosentino et al., 2020e).

## References

- Baker, A. R., Jickells, T. D., Witt, M., & Linge, K. L. (2006). Trends in the solubility of iron, aluminium, manganese and phosphorus in aerosol collected over the Atlantic Ocean. *Marine Chemistry*, 98, 43-58. doi:10.1016/j.marchem.2005.06.004.
- Baker, A. R., Weston, K., Kelly, S. D., Voss, M., Streu, P., & Cape, J. N. (2007). Dry and wet deposition of nutrients from the tropical Atlantic atmosphere: Links to primary productivity and nitrogen fixation. *Deep Sea Research Part I: Oceanographic Research Papers*, 54(10), 1704-1720. doi:10.1016/j.dsr.2007.07.001.

- Baker, A. R., & Croot, P. L. (2010). Atmospheric and marine controls on aerosol iron solubility in seawater. *Marine Chemistry*, 120(1-4), 4-13. doi:10.1016/j.marchem.2008.09.003.
- Baker, A. R., Adams, C., Bell, T. G., Jickells, T. D., & Ganzeveld, L. (2013). Estimation of atmospheric nutrient inputs to the Atlantic Ocean from 50° N to 50° S based on large-scale field sampling: Iron and other dust-associated elements. *Global Biogeochemical Cycles*, 27(3), 755-767. doi:10.1002/gbc.20062.
- Barré, N., Provost, C., Sennechael, N., & Lee, J. H. (2008). Circulation in the Ona Basin, southern Drake Passage. *Journal of Geophysical Research: Oceans*, 113(C4). doi.org/10.1029/2007JC004549.
- Bia, G., Borgnino, L., Zampieri, G., & García, M. G. (2020). Fluorine surface speciation in South Andean volcanic ashes. *Chemical Geology*, 532, 119402. doi:10.1016/J.CHEMGEO.2019.119402.
- Biesinger, M. C., Payne, B. P., Grosvenor, A. P., Lau, L. W., Gerson, A. R., & Smart, R. S. C. (2011). Resolving surface chemical states in XPS analysis of first row transition metals, oxides and hydroxides: Cr, Mn, Fe, Co and Ni. *Applied Surface Science*, 257(7), 2717-2730. doi:10.1016/j.apsusc.2010.10.051.
- Bishop, J. K. B., Davis, R. E., & Sherman, J. T. (2002). Robotic observations of dust storm enhancement of carbon biomass in the North Pacific. *Science*, 298(5594), 817-821. doi:10.1126/science.1074961.
- Bonnet, S., Guieu, C., Bruyant, F., Prášil, O., Van Wambeke, F., Raimbault, P., et al. (2008). Nutrient limitation of primary productivity in the Southeast Pacific (BIOSOPE cruise). *Biogeosciences*, 5(1), 215-225.
- Boyd, P. W., McTainsh, G., Sherlock, V., Richardson, K., Nichol, S., Ellwood, M., & Frew, R. (2004). Episodic enhancement of phytoplankton stocks in New Zealand subantarctic waters: Contribution of atmospheric and oceanic iron supply. *Global Biogeochemical Cycles*, 18(GB1029). doi:10.1029/2002GB002020.
- Boyd, P. W., & Mackie, D. (2008). Comment on the Southern Ocean biological response to aeolian iron deposition. *Science*, 319(5860), 159a. doi:10.1126/science.1149884.
- Boyd, P. W., Mackie, D. S., & Hunter, K. A. (2010). Aerosol iron deposition to the surface ocean - Modes of iron supply and biological responses. *Marine Chemistry*, 120, 128-143. doi:10.1016/J.MARCHEM.2009.01.008.
- Bucher, E. H., & Stein, A. F. (2016). Large salt dust storms follow a 30-year rainfall cycle in the Mar Chiquita lake (Córdoba, Argentina). *PLoS ONE*, 11(6), e0156672. doi:10.1371/journal.pone.0156672.
- Bullard, J. E., Baddock, M., Bradwell, T., Crusius, J., Darlington, E., Gaiero, D., et al. (2016). High-latitude dust in the Earth system. *Reviews of Geophysics*, 54(2), 447-485. doi:10.1002/2016RG000518.
- Carranza, M. M., Gille, S. T., Piola, A. R., Charo, M., & Romero, S. I. (2017). Wind modulation of upwelling at the shelf-break front off Patagonia: Observational evidence. *Journal of Geophysical Research: Oceans*, 122(3), 2401-2421. doi:10.1002/2016JC012059.
- Cassar, N., Bender, M. L., Barnett, B. A., Fan, S., Moxim, W. J., Levy II, H., & Tilbrook, B. (2007). The southern ocean biological response to aeolian iron deposition. *Science*, 317(5841), 1067-1070. doi:10.1126/science.1144602.

- Colin, J. L., Jaffrezo, J. L., & Gros, J. M. (1990). Solubility of major species in precipitation: Factors of variation. *Atmospheric Environment. Part A. General Topcis*, 24(3), 537–544. doi:10.1016/0960-1686(90)90008-B.
- Cosentino, N. J., Gaiero D. M., Torre, G., Pasquini, A. I., Coppo, R., Arce, J. M., & Vélez, G. (2020a). Atmospheric dust dynamics in southern South America: A 14-year modern dust record in the loessic Pampean region. *The Holocene* 30(4): 575-588. doi:10.1177/0959683619875198.
- Cosentino, N. J., Ruiz-Etcheverry, L. A., Bia, G. L., Simonella, L. E., Coppo, R., Torre, G. et al. (2020b). Total iron content in dust samples of southernmost Patagonia. Interdisciplinary Earth Data Alliance (IEDA). doi:10.26022/IEDA/111753. Accessed 18 November 2020.
- Cosentino, N. J., Ruiz-Etcheverry, L. A., Bia, G. L., Simonella, L. E., Coppo, R., Torre, G. et al. (2020c). Deionized water and acid solubility of iron in southernmost Patagonian dust samples. Interdisciplinary Earth Data Alliance (IEDA). doi:10.26022/IEDA/111754. Accessed 18 November 2020.
- Cosentino, N. J., Ruiz-Etcheverry, L. A., Bia, G. L., Simonella, L. E., Coppo, R., Torre, G. et al. (2020d). Decadal dust monitoring in southernmost Patagonia. Interdisciplinary Earth Data Alliance (IEDA). doi:10.26022/IEDA/111756. Accessed 18 November 2020.
- Cosentino, N. J., Ruiz-Etcheverry, L. A., Bia, G. L., Simonella, L. E., Coppo, R., Torre, G. et al. (2020e). Surface iron speciation of dust samples in southernmost Patagonia. Interdisciplinary Earth Data Alliance (IEDA). doi:10.26022/IEDA/111755. Accessed 18 November 2020.
- Crespi-Abril, A. C., Soria, G., De Cian, A., & López-Moreno, C. (2018). Roaring forties: An analysis of a decadal series of data of dust in Northern Patagonia. *Atmospheric Environment*, 177, 111–119. doi:10.1016/J.ATMOSENV.2017.11.019.
- Crispo, S. M., Peterson, T. D., & Lohan, M. C. (2005). Implications of an Asian dust storm on the Gulf of Alaska. *Sea Technology*, 46(9), 29-35.
- Cwiertny, D. M., Baltrusaitis, J., Hunter, G. J., Laskin, A., Scherer, M. M., & Grassian, V. H. (2008). Characterization and acid-mobilization study of iron-containing mineral dust source materials. *Journal of Geophysical Research: Atmospheres*, 113(D5). doi:10.1029/2007JD009332.
- Draxler, R. R., & Hess, G. D. (1998). An overview of the HYSPLIT\_4 modelling system for trajectories, dispersion and deposition. *Australian Meteorological Magazine*, 47, 295-308.
- Duce, R. A., & Tindale, N. W. (1991). Atmospheric transport of iron and its deposition in the ocean. *Limnology and Oceanography*, 36(8), 1715–1726. doi:10.4319/lo.1991.36.8.1715.
- Epstein, M. S., Diamondstone, B. I., & Gills, T. E. (1989). A new river sediment standard reference material. *Talanta*, 36(1-2), 141-150.
- Erickson III, D. J., Hernandez, J. L., Ginoux, P., Gregg, W. W., McClain, C., & Christian, J. (2003). Atmospheric iron delivery and surface ocean biological activity in the Southern Ocean and Patagonian region. *Geophysical Research Letters*, 30(12), 1609. doi:10.1029/2003GL017241.
- Ferrari, R., Provost, C., Renault, A., Sennéchaël, N., Barré, N., Park, Y. H., & Lee, J. H. (2012). Circulation in Drake Passage revisited using new current time series and satellite altimetry: 1. The Yaghan Basin. *Journal of Geophysical Research: Oceans*, 117(C12). doi:10.1029/2012JC008264.

- Fryrear, D. W. (1986). A field dust sampler. *Journal of Soil and Water Conservation*, 41, 117–120.
- Gaiero, D. M., Probst, J.-L., Depetris, P. J., Bidart, S. M., & Leleyter, L. (2003). Iron and other transition metals in Patagonian riverborne and windborne materials: Geochemical control and transport to the southern South Atlantic Ocean. *Geochimica et Cosmochimica Acta*, 67(19), 3603–3623. doi:10.1016/S0016-7037(03)00211-4.
- Gaiero, D. M., Simonella, L. E., Gassó, S., Gili, S., Stein, A. F., Sosa, P., et al. (2013). Ground/satellite observations and atmospheric modeling of dust storms originating in the high Puna-Altiplano deserts (South America): Implications for the interpretation of paleoclimatic archives. *Journal of Geophysical Research: Atmospheres*, 118, 1–15. doi:10.1002/JGRD.50036.
- Gallissai, R., Volpe, G., & Peters, F. (2016). Large Saharan dust storms: Implications for chlorophyll dynamics in the Mediterranean Sea. *Global Biogeochemical Cycles*, 30(11), 1725–1737. doi:10.1002/2016GB005404.
- Gassó, S., Stein, A., Marino, F., Castellano, E., Udisti, R., & Ceratto, J. (2010). A combined observational and modeling approach to study modern dust transport from the Patagonia desert to East Antarctica. *Atmospheric Chemistry and Physics*, 10, 8287–8303. doi:10.5194/ACP-10-8287-2010.
- Gassó, S., & Torres, O. (2019). Temporal characterization of dust activity in the Central Patagonia desert (years 1964–2017). *Journal of Geophysical Research: Atmospheres*, 124. doi:10.1029/2018JD030209.
- Geider, R. J., MacIntyre, H. L., & Kana, T. M. (1997). Dynamic model of phytoplankton growth and acclimation: responses of the balanced growth rate and the chlorophyll a: carbon ratio to light, nutrient-limitation and temperature. *Marine Ecology Progress Series*, 148, 187–200. doi:10.3354/meps148187.
- Gili, S., Gaiero, D. M., Goldstein, S. L., Chemale Jr, F., Jweda, J., Kaplan, M. R., et al. (2017). Glacial/interglacial changes of Southern Hemisphere wind circulation from the geochemistry of South American dust. *Earth and Planetary Science Letters*, 469, 98–109. doi:10.1016/j.epsl.2017.04.007.
- Gillette, D. A., Adams, J., Endo, A., & Smith, D. (1980). Threshold velocities for input of soil particles into the air by desert soils. *Journal of Geophysical Research*, 85, 5621–5630.
- Goossens, D., & Offer, Z. (2000). Wind tunnel and field calibration of six aeolian dust samplers. *Atmospheric Environment*, 34, 1043–1057.
- Grosvenor, A. P., Kobe, B. A., Biesinger, M. C., & McIntyre, N. S. (2004). Investigation of multiplet splitting of Fe 2p XPS spectra and bonding in iron compounds. *Surface and Interface Analysis*, 36(12), 1564–1574. doi:10.1002/sia.1984.
- Guiéu, C., Loÿe-Pilot, M. D., Ridame, C., & Thomas, C. (2002). Chemical characterization of the Saharan dust end-member: Some biogeochemical implications for the western Mediterranean Sea. *Journal of Geophysical Research: Atmospheres*, 107(D15), ACH 5-1-ACH 5-11. doi:10.1029/2001JD000582.
- Hand, J. L., Mahowald, N. M., Chen, Y., Siefert, R. L., Luo, C., Subramaniam, A., & Fung, I. (2004). Estimates of atmospheric-processed soluble iron from observations and a global mineral aerosol model: biogeochemical implications. *Journal of Geophysical Research: Atmospheres*, 109(D17). doi:10.1029/2004JD004574.

Huot, Y., Babin, M., Bruyant, F., Grob, C., Twardowski, M. S., & Claustre, H. (2007). Does chlorophyll a provide the best index of phytoplankton biomass for primary productivity studies? *Biogeosciences Discussions*, 4(2), 707-745.

Kanamitsu, M. (1989). Description of the NMC Global Data Assimilation and Forecast System. *Weather and Forecasting*, 4, 335-342.

Koch, D., Jacob, D., Tegen, I., Rind, D., & Chin, M. (2000). Tropospheric sulfur simulation and sulfate direct radiative forcing in the Goddard Institute for Space Studies general circulation model. *Journal of Geophysical Research: Atmospheres*, 104(D19), 23799–23822. doi:10.1029/1999JD900248.

Koenig, Z., Provost, C., Ferrari, R., Sennéchaël, N., & Rio, M. H. (2014). Volume transport of the Antarctic Circumpolar Current: Production and validation of a 20 year long time series obtained from in situ and satellite observations. *Journal of Geophysical Research: Oceans*, 119(8), 5407-5433. doi:10.1002/2014JC009966.

Johnson, K. S., Elrod, V. A., Fitzwater, S. E., Plant, J. N., Chavez, F. P., Tanner, S. J., et al. (2003). Surface ocean-lower atmosphere interactions in the northeast Pacific Ocean gyre: Aerosols, iron, and the ecosystem response. *Global Biogeochemical Cycles*, 17(2). doi:10.1029/2002GB002004.

Journet, E., Desboeufs, K. V., Caquineau, S., & Colin, J. L. (2008). Mineralogy as a critical factor of dust iron solubility. *Geophysical Research Letters*, 35(7). doi.org/10.1029/2007GL031589.

Lawrence, C. R., & Neff, J. C. (2009). The contemporary physical and chemical flux of aeolian dust: A synthesis of direct measurements of dust deposition. *Chemical Geology*, 267, 46–63. doi:10.1016/J.CHEMGEO.2009.02.005.

Li, F., Ginoux, P., & Ramaswamy, V. (2008). Distribution, transport, and deposition of mineral dust in the Southern Ocean and Antarctica: Contribution of major sources. *Journal of Geophysical Research*, 113(D10207). doi:10.1029/2007JD009190.

Mackie, D. S., Boyd, P. W., McTainsh, G. H., Tindale, N. W., Westberry, T. K., & Hunter, K. A. (2008). Biogeochemistry of iron in Australian dust: From eolian uplift to marine uptake. *Geochemistry, Geophysics, Geosystems*, 9(3). doi:10.1029/2007GC001813.

Mahowald, N. M., Baker, A. R., Bergametti, G., Brooks, N., Duce, R. A., Jickells, et al. (2005). Atmospheric global dust cycle and iron inputs to the ocean. *Global Biogeochemical Cycles*, 19(GB4025). doi:10.1029/2004GB002402.

Maldonado, M. T., & Price, N. M. (1999). Utilization of iron bound to strong organic ligands by plankton communities in the subarctic Pacific Ocean. *Deep Sea Research Part II: Topical Studies in Oceanography*, 46(11-12), 2447-2473. doi:10.1016/S0967-0645(99)00071-5.

Martin, J. H. (1990). Glacial-interglacial CO<sub>2</sub> change: the iron hypothesis. *Paleoceanography and paleoclimatology*, 5(1), 1–13. doi:10.1029/PA005i001p00001.

Matano, R. P., & Palma, E. D. (2008). On the upwelling of downwelling currents. *Journal of Physical Oceanography*, 38(11), 2482-2500. doi:10.1175/2008JPO3783.1.

Meskhidze, N., Chameides, W. L., Nenes, A., & Chen, G. (2003). Iron mobilization in mineral dust: Can anthropogenic SO<sub>2</sub> emissions affect ocean productivity? *Geophysical Research Letters*, 30(21). doi:10.1029/2003GL018035.

- Meskhidze, N., Chameides, W. L., & Nenes, A. (2005). Dust and pollution: A recipe for enhanced ocean fertilization? *Journal of Geophysical Research: Atmospheres*, 110(D3). doi:10.1029/2004JD005082.
- Meskhidze, N., Nenes, A., Chameides, W. L., Luo, C., & Mahowald, N. (2007). Atlantic Southern Ocean productivity: Fertilization from above or below? *Global Biogeochemical Cycles*, 21(2). doi:10.1029/2006GB002711.
- Mills, M. M., Ridame, C., Davey, M., La Roche, J., & Geider, R. J. (2004). Iron and phosphorus co-limit nitrogen fixation in the eastern tropical North Atlantic. *Nature*, 429, 292-294. doi:10.1038/nature02550.
- Moore, J. K., Doney, S. C., Glover, D. M., & Fung, I. Y. (2001). Iron cycling and nutrient-limitation patterns in surface waters of the World Ocean. *Deep Sea Research Part II: Topical Studies in Oceanography*, 49(1-3), 463-507. doi:10.1016/S0967-0645(01)00109-6.
- Moore, C. M., Mills, M. M., Milne, A., Langlois, R., Achterberg, E. P., Lochte, K., et al. (2006). Iron limits primary productivity during spring bloom development in the central North Atlantic. *Global Change Biology*, 12(4), 626-634. doi:10.1111/j.1365-2486.2006.01122.x.
- Morel, F. M. M., Kustka, A. B., & Shaked, Y. (2008). The role of unchelated Fe in the iron nutrition of phytoplankton. *Limnology and Oceanography*, 53, 400-404. doi:10.4319/lo.2008.53.1.0400.
- Neff, P. D., & Bertler, N. A. N. (2015). Trajectory modeling of modern dust transport to the Southern Ocean and Antarctica, *Journal of Geophysical Research: Atmosphere*, 120, 9303-9322. doi:10.1002/2015JD023304.
- Ohgaito, R., Abe-Ouchi, A., O'ishi, R., Takemura, T., Ito, A., Hajima, T., et al. (2018). Effect of high dust amount on surface temperature during the Last Glacial Maximum: a modelling study using MIROC-ESM. *Climate of the Past*, 14, 1565-1581. doi:10.5194/cp-14-1565-2018.
- Orange, D., Gac, J.-Y., Probst J.-L., & Tanre, D. (1990). Mesure du dépôt au sol des aérosols désertiques. Une méthode simple de prélèvement : le capteur pyramidal. *Comptes Rendus de l'Académie des Sciences*, 311(2), 167-172.
- Palma, E. D., Matano, R. P., & Piola, A. R. (2008). A numerical study of the Southwestern Atlantic Shelf circulation: Stratified ocean response to local and offshore forcing. *Journal of Geophysical Research: Oceans*, 113(C11). doi:10.1029/2007JC004720.
- Paparazzo, F. E., Crespi-Abril, A. C., Gonçalves, R. J., Barbieri, E. S., Gracia Villalobos, L. L., Solís, M. E., & Soria, G. (2018). Patagonian dust as a source of macronutrients in the Southwest Atlantic Ocean. *Oceanography*, 31(4), 33-39. doi:10.5670/oceanog.2018.408.
- Perron, M. M. G., Strzelec, M., Gault-Ringold, M., Proemse, B. C., Boyd, P. W., & Bowie, A. R. (2020). Assessment of leaching protocols to determine the solubility of trace metals in aerosols. *Talanta*, 208, 120377. doi:10.1016/j.talanta.2019.120377.
- Rivas, A. L. (1997). Current meter observations in the Argentine Continental Shelf. *Continental Shelf Research*, 17, 391-406. doi:10.1016/S0278-4343(96)00039-8.
- Rivas, A. L., & Piola, A. R. (2002). Vertical stratification at the shelf off northern Patagonia. *Continental Shelf Research*, 22(10), 1549-1558. doi:10.1016/S0278-4343(02)00011-0.

- Rivas, A. L., & Pisoni, J. P. (2009). Identification, characteristics and seasonal evolution of surface thermal fronts in the Argentinean Continental Shelf. *Journal of Marine Systems*, 79(1-2), 134–143. doi:10.1016/j.jmarsys.2009.07.008.
- Romero, S. I., Piola, A. R., Charo, M., & Garcia, C. A. E. (2006). Chlorophyll-a variability off Patagonia based on SeaWiFS data. *Journal of Geophysical Research: Oceans*, 111(C5). doi:10.1029/2005JC003244.
- Saraceno, M., Provost, C., & Piola, A. R. (2005). On the relationship of satellite retrieved surface temperature fronts and chlorophyll-a in the Western South Atlantic. *Journal of Geophysical Research: Oceans*, 110, C11016, doi:10.1029/2004JC002736.
- Saraceno, M., & Provost, C. (2012). On eddy polarity distribution in the Southwestern Atlantic. *Deep Sea Research I*, 69, 62-69. doi:10.1016/j.dsr.2012.07.005.
- Sathyendranath, S., Brewin, R. J., Brockmann, C., Brotas, V., Calton, B., Chuprin, A., et al. (2019). An ocean-colour time series for use in climate studies: The experience of the Ocean-Colour Climate Change Initiative (OC-CCI). *Sensors*, 19(19), 4285. doi:10.3390/s19194285.
- Schlitzer, R., Anderson, R. F., Dodas, E. M., Lohan, M., Geibert, W., Tagliabue, A., et al. (2018). The GEOTRACES intermediate data product 2017. *Chemical Geology*, 493, 210-223. doi:10.1016/J.CHEMGEO.2018.05.040.
- Schroth, A. W., Crusius, J., Sholkovitz, E. R., & Bostick, B. C. (2009). Iron solubility driven by speciation in dust sources to the ocean. *Nature Geoscience*, 2(5), 337-340. doi:10.1038/ngeo501.
- Sedwick, P. N., Church, T. M., Bowie, A. R., Marsay, C. M., Ussher, S. J., Achilles, K. M., et al. (2005). Iron in the Sargasso Sea (Bermuda Atlantic Time-series Study region) during summer: Eolian imprint, spatiotemporal variability, and ecological implications. *Global Biogeochemical Cycles*, 19(4). doi:10.1029/2004GB002445.
- Shaked, Y., Kustka, A. B., & Morel, F. M. (2005). A general kinetic model for iron acquisition by eukaryotic phytoplankton. *Limnology and Oceanography*, 50(3), 872-882. doi:10.4319/lo.2005.50.3.0872.
- Shaw, E. C., Gabric, A. J., & McTainsh, G. H. (2008). Impacts of aeolian dust deposition on phytoplankton dynamics in Queensland coastal waters. *Marine and Freshwater Research*, 59(11), 951-962. doi:10.1071/MF08087.
- Shoenfelt, E. M., Sun, J., Winckler, G., Kaplan, M. R., Borunda, A. L., Farrell, K. R., et al. (2017). High particulate iron (II) content in glacially sourced dusts enhances productivity of a model diatom. *Science advances*, 3(6), e1700314. doi:10.1126/sciadv.1700314.
- Simonella, L. E., Gaiero, D. M., & Palomeque, M. E. (2014). Validation of a continuous flow method for the determination of soluble iron in atmospheric dust and volcanic ash. *Talanta*, 128, 248-253. doi:10.1016/J.TALANTA.2014.04.076.
- Simonella, L. E., Palomeque, M. E., Croot, P. L., Stein, A., Kupczewski, M., Rosales, A., et al. (2015). Soluble iron inputs to the Southern Ocean through recent andesitic to rhyolitic volcanic ash eruptions from the Patagonian Andes. *Global Biogeochemical Cycles*, 29, 1125-1144. doi:10.1002/2015GB005177.
- Skonieczny, C., Bory, A., Bout-Roumazielles, V., Abouchami, W., Galer, S. J. G., Crosta, X., et al. (2011). The 7–13 March 2006 major Saharan outbreak: Multi-proxy characterization of mineral dust deposited on the West African margin. *Journal of Geophysical Research*, 116(D18). doi:10.1029/2011JD016173.

- Song, H., Marshall, J., Follows, M. J., Dutkiewicz, S., & Forget, G. (2016). Source waters for the highly productive Patagonian shelf in the southwestern Atlantic. *Journal of Marine Systems*, 158, 120-128. doi:10.1016/J.MARSYS.2016.02.009.
- Strzepek, R. F., Maldonado, M. T., Hunter, K. A., Frew, R. D., & Boyd, P. W. (2011). Adaptive strategies by Southern Ocean phytoplankton to lessen iron limitation: Uptake of organically complexed iron and reduced cellular iron requirements. *Limnology and Oceanography*, 56(6), 1983-2002. doi:10.4319/lo.2011.56.6.1983.
- Takemura, T., Egashira, M., Matsuzawa, K., Ichijo, H., O'ishi, R., & Abe-Ouchi, A. (2009). A simulation of the global distribution and radiative forcing of soil dust aerosols at the Last Glacial Maximum. *Atmospheric Chemistry and Physics*, 9, 3061-3073. doi:10.5194/acp-9-3061/2009.
- Tian, R., Chen, J., Sun, X., Li, D., Liu, C., & Weng, H. (2018). Algae explosive growth mechanism enabling weather-like forecast of harmful algal blooms. *Scientific Reports*, 8, 9923. doi:10.1038/s41598-018-28104-7.
- Torfstein, A., & Kienast, S. S. (2018). No Correlation Between Atmospheric Dust and Surface Ocean Chlorophyll-a in the Oligotrophic Gulf of Aqaba, Northern Red Sea. *Journal of Geophysical Research: Biogeosciences*, 123(2), 391-405. doi:10.1002/2017JG004063.
- Villarreal, M. L., & Coronato, A. (2017). Characteristics and nature of pans in the semi-arid temperate/cold steppe of Tierra del Fuego, In *Advances in Geomorphology and Quaternary Studies in Argentina* (pp. 203-224). Springer, Cham.
- Wagner, C. D., Riggs, W. M., Davis, L. E., Moulder, J. F., & Muilenberg, G. E. (1997). *Handbook of X-Ray Photoelectron Spectroscopy*. Perkin-Elmer Corporation, Physical Electronics Division: Eden Prairie, MN.
- Walter, H. J., Hegner, E., Diekmann, B., & Kuhn, G. (2000). Provenance and transport of terrigenous sediment in the South Atlantic Ocean and their relations to glacial and interglacial cycles: Nd and Sr isotopic evidence. *Geochimica et Cosmochimica Acta*, 64(22), 3813-3827. doi:10.1016/S0016-7037(00)00476-2.
- Waza, A., Schneiders, K., May, J., Rodríguez, S., Epple, B., & Kandler, K. (2019). Field comparison of dry deposition samplers for collection of atmospheric mineral dust: results from single-particle characterization. *Atmospheric Measurement Techniques*, 12, 6647-6665. doi:10.5194/AMT-12-6647-2019.
- Westberry, T. K., Siegel, D. A., & Subramaniam, A. (2005). An improved bio-optical model for the remote sensing of *Trichodesmium* spp. blooms. *Journal of Geophysical Research: Oceans*, 110(C6). doi:10.1029/2004JC002517.
- Wilson, S. A. (1998). Data compilation for USGS reference material GSP-2, Granodiorite, Silver Plume, Colorado. *US Geological Survey Open File Rep.*
- Young, R. W., Carder, K. L., Betzer, P. R., Costello, D. K., Duce, R. A., DiTullio, G. R., et al. (1991). Atmospheric iron inputs and primary productivity: Phytoplankton responses in the North Pacific. *Global Biogeochemical Cycles*, 5(2), 119-134. doi:10.1029/91GB00927.
- Yukimoto, S., Adachi, Y., Hosaka, M., Sakami, T., Yoshimura, H., Hirabara, M., et al. (2012). A new global climate model of the Meteorological Research Institute: MRI-CGCM3—model description and basic performance—. *Journal of the Meteorological Society of Japan*, 90, 23-64. doi:10.2151/jmsj.2012-A02.